JCB

Article

Spatiotemporal organization of exocytosis emerges during neuronal shape change

Fabio L. Urbina,[1] Shawn M. Gomez,[4] and Stephanie L. Gupton[1,2,3]

[1]Department of Cell Biology and Physiology, [2]Neuroscience Center, and [3]Lineberger Comprehensive Cancer Center, University of North Carolina at Chapel Hill, Chapel Hill, NC
[4]University of North Carolina at Chapel Hill/North Carolina State University Joint Department of Biomedical Engineering, University of North Carolina at Chapel Hill/North Carolina State University, Chapel Hill, NC

Neurite elongation and branching in developing neurons requires plasmalemma expansion, hypothesized to occur primarily via exocytosis. We posited that exocytosis in developing neurons and nonneuronal cells would exhibit distinct spatiotemporal organization. We exploited total internal reflection fluorescence microscopy to image vesicle-associated membrane protein (VAMP)–pHluorin—mediated exocytosis in mouse embryonic cortical neurons and interphase melanoma cells, and developed computer-vision software and statistical tools to uncover spatiotemporal aspects of exocytosis. Vesicle fusion behavior differed between vesicle types, cell types, developmental stages, and extracellular environments. Experiment-based mathematical calculations indicated that VAMP2-mediated vesicle fusion supplied excess material for the plasma membrane expansion that occurred early in neuronal morphogenesis, which was balanced by clathrin-mediated endocytosis. Spatial statistics uncovered distinct spatiotemporal regulation of exocytosis in the soma and neurites of developing neurons that was modulated by developmental stage, exposure to the guidance cue netrin-1, and the brain-enriched ubiquitin ligase tripartite motif 9. In melanoma cells, exocytosis occurred less frequently, with distinct spatial clustering patterns.

Introduction

Exocytosis is a fundamental behavior, ubiquitous across eukaryotes and cell types. Vesicle fusion promotes secretion of biomolecules and insertion of transmembrane proteins and lipids into the plasma membrane, which can affect physiological processes including polarized growth and motility (Mostov et al., 2000; Winkle et al., 2014). Where and when vesicle fusion occurs may be a critical regulatory point in cellular physiology. The minimal machinery required for fusion is the SNARE complex (Söllner et al., 1993), comprising a tightly associated bundle of four α-helical coiled-coils (CCs). For exocytosis, one α-helix is provided by a vSNARE, such as vesicle-associated membrane protein (VAMP) 2 (synaptobrevin), VAMP3, or VAMP7 (tetanus-insensitive VAMP) in mammals or snc1/2 in yeast (McMahon et al., 1993; Protopopov et al., 1993; Galli et al., 1998). Other α-helixes are provided by plasma membrane target (t)-SNAREs—syntaxin-1 and synaptosomal-associated protein 25 (SNAP25)—in mammals or Sso1p/Sso2p and sec9 in yeast (Aalto et al., 1993; Söllner et al., 1993; Brennwald et al., 1994).

VAMP2, SNAP25, and syntaxin-1 were identified in brain, where they mediate synaptic vesicle fusion and neurotransmitter release. VAMP7 functions in SNARE-mediated exocytosis in both neurons and nonneuronal cells (Galli et al., 1998; Martinez-Arca et al., 2000). Subsequent to synaptic vesicle release, clathrin-dependent endocytic retrieval of membrane material maintains membrane homeostasis (Heuser and Reese, 1973; Pearse, 1976). Perhaps less appreciated than synaptic exocytosis is the developmental exocytosis that occurs before synaptogenesis. The acquisition of an elongated, complex neuronal morphology entails significant plasma membrane expansion, estimated at 20% per day (Pfenninger, 2009). This is remarkable when compared with concomitant neuronal volume increases estimated at less than 1%. We previously demonstrated that constitutive SNARE-mediated exocytosis is required during neuritogenesis and axon branching (Gupton and Gertler, 2010; Winkle et al., 2014). We hypothesize exocytosis provides membrane material to the expanding plasma membrane, which can only stretch 2–3% before rupturing (Bloom et al., 1991), however whether SNARE-mediated exocytosis supplies sufficient material for membrane expansion has not been addressed. Asymmetric exocytosis is linked to attractive axonal turning (Tojima et al., 2007, 2014; Ros et al., 2015). As several neurological disorders are accompanied by disrupted neuronal morphology (Paul et al., 2007; Engle, 2010), regulated exocytosis involved in appropriate neuronal morphogenesis is likely central to the formation and maintenance of a functional nervous system. However, how exocytosis is spatially and temporally organized in developing neurons is not known.

Correspondence to Stephanie L. Gupton: sgupton@email.unc.edu

The Rockefeller University Press
J. Cell Biol. Vol. 217 No. 3 1113–1128
https://doi.org/10.1083/jcb.201709064

To visualize exocytic vesicle fusion, here we exploited the pH-sensitive variant of GFP (pHluorin) attached to the lumenal side of a v-SNARE, which illuminates the occurrence of fusion pore opening between the acidic vesicular lumen and the neutral extracellular environment (Miesenböck et al., 1998). Analysis of such images has remained a manual and potentially biased time-intensive process. Here we developed computer-vision software and statistical methods for unbiased automated detection and analysis of VAMP-pHluorin–mediated exocytosis. This uncovered spatial and temporal organization and regulation of exocytosis in developing neurons that were distinct in soma and neurites, modulated by the developmental stage of the neuron, and sensitive to the axon guidance cue netrin-1. Mathematical estimates based on empirical findings suggested that VAMP2-mediated exocytosis and clathrin-mediated endocytosis approximately describe membrane expansion in developing neurons. Compared with neurons, melanoma cells exhibited slower frequencies and a distinct organization of exocytosis.

Results

Automated identification and analysis of exocytosis

Whether exocytosis is sufficient for neuronal plasmalemmal expansion, how fusion is organized spatially and temporally, and the mechanisms that regulate developmental exocytosis are not established. We imaged VAMP2-pHluorin or VAMP7-pHluorin in mouse embryonic cortical neurons using widefield epifluorescence or total internal reflection fluorescence (TIRF) microscopy to visualize exocytosis (Fig. S1 A). The area-corrected frequency of VAMP2-mediated exocytosis at the basal plasma membrane measured from the TIRF images was ∼1.4-fold higher than measured by widefield microscopy, which captures events at both basal and apical membranes (Fig. S1 B). In contrast, the frequency of VAMP7-mediated exocytosis was comparable between the two imaging modes (Fig. S1 B). VAMP2-pHluorin exhibited a higher plasma membrane fluorescence than VAMP7-pHluorin (Fig. S1 C), which may occlude identification of apical VAMP2-mediated events. Indeed, events at the apex of the soma were visible by widefield microscopy only when the focal plane was shifted (Fig. S1 D, black arrows). This suggests that VAMP2-mediated events were not captured simultaneously on both membranes, and that the frequency of fusion observed by widefield microscopy was an underestimation. We conclude that the frequency of exocytosis is comparable between apical and basal plasma membranes for both VAMP2- and VAMP7-mediated exocytosis (Fig. S1, B and D), and was best captured by TIRF microscopy. For subsequent analysis, we relied on TIRF microscopy, which also offered increased signal-to-noise and spatial resolution, reduced photobleaching and phototoxicity, and faster image acquisition.

To perform unbiased, efficient identification and analysis of VAMP2-pHluorin–mediated exocytosis from TIRF images, we developed a computer-vision–based approach implemented in MATLAB and R (Fig. 1 A, Video 1, and supplemental .m and .R files). In the analysis pipeline, the cell was identified and segmented from noncellular background and a single cell mask was created, as cells did not significantly change shape or size over imaging (∼2 min). We developed an algorithm that detected both diffraction-limited and larger fluorescent objects (Fig. 1 A; see Materials and methods). To assemble a coherent picture of exocytic events over time, fluorescent objects representing individual vesicles that may be undergoing exocytosis are linked across frames using a Kalman filter (Kalman, 1960; Fig. 1 B and Fig. S2 A). The Kalman filter used a cost matrix to determine whether an object detected in one frame was a new object, i.e., a fusion pore opening, or an existing object, i.e., the continuation of an exocytic event. Critically, the Kalman filter can handle the linkage of both motile objects, such as a motile fluorescent vesicle, and nonmotile objects, such as a fusing vesicle. Bona fide exocytic events were defined as transient, nonmotile objects that reached a significant intensity above the mean local background intensity calculated from previous frames, followed by an exponential fluorescence decay, with no limit on how long an event could last (Fig. 1 C; see Materials and methods).

Confirmation of exocytic detection

To test the algorithm accuracy at identifying transient events, neurons were treated with NH_4Cl (Fig. 1 D and Video 2), which alkalinizes intracellular vesicular compartments, reversing quenching of pHluorin fluorescence (Miesenböck et al., 1998). NH_4Cl treatment increased vesicular fluorescence (Fig. 1 D), and events detected were near or at zero, indicating the algorithm identified only transient fluorescent exocytic events. To confirm identified events were VAMP2-dependent, neurons were treated with tetanus neurotoxin (TeNT), which cleaves the cytoplasmic face of VAMP2, preventing SNARE complex formation and fusion (Link et al., 1992). VAMP2-pHluorin–mediated fusion events were rarely detected, if at all, indicating that the algorithm identified TeNT-sensitive events (Fig. 1 D and Video 2). To ensure images were acquired at a sufficient frame rate to capture all events, we artificially decreased sampling. At an acquisition rate of 1 Hz, the frequency of detected events was underestimated as compared with 5 Hz; no further improvement occurred at 10 Hz (Fig. 1 E). We subsequently used an acquisition rate of 10 Hz to satisfy the Nyquist criterion and ensure ample resolution for analyses of individual exocytic events. To assess the robustness of the algorithm to local background variation caused by plasma membrane–localized VAMP2-pHluorin and system noise, and to calculate true error rates, computer simulations of exocytic events based on empirical measurements were created (Fig. 1 F; see Materials and methods). The detection software was robust to the typical signal-to-noise ratio observed experimentally, with an error rate 2–7% (Fig. 1 G), comparable or better than other algorithms (Sebastian et al., 2006; Yuan et al., 2015).

A series of measurements were made to describe the population of fusing vesicles (Fig. 1, H–L), including the frequency of exocytosis per neuron (Fig. 1 I); the peak change in fluorescence per event (ΔF/F; Fig. 1, H and J), which estimates the amount of VAMP2-pHluorin per vesicle; the event $t_{1/2}$ (Fig. 1, H and K), which represents how quickly the VAMP2-pHluorin fluorescence decayed; the shape of the initial exocytic boundary (major/minor axis; Fig. 1 L), and the time and location (x, y) of fusion. The shape of the $t_{1/2}$ distribution exhibited no artificial truncation, indicating events with short or long $t_{1/2}$ were detected. The frequency of VAMP2-pHluorin exocytic events detected from TIRF images by the software was not different from that counted by several independent trained users (Fig. 1 I; $P = 0.56$).

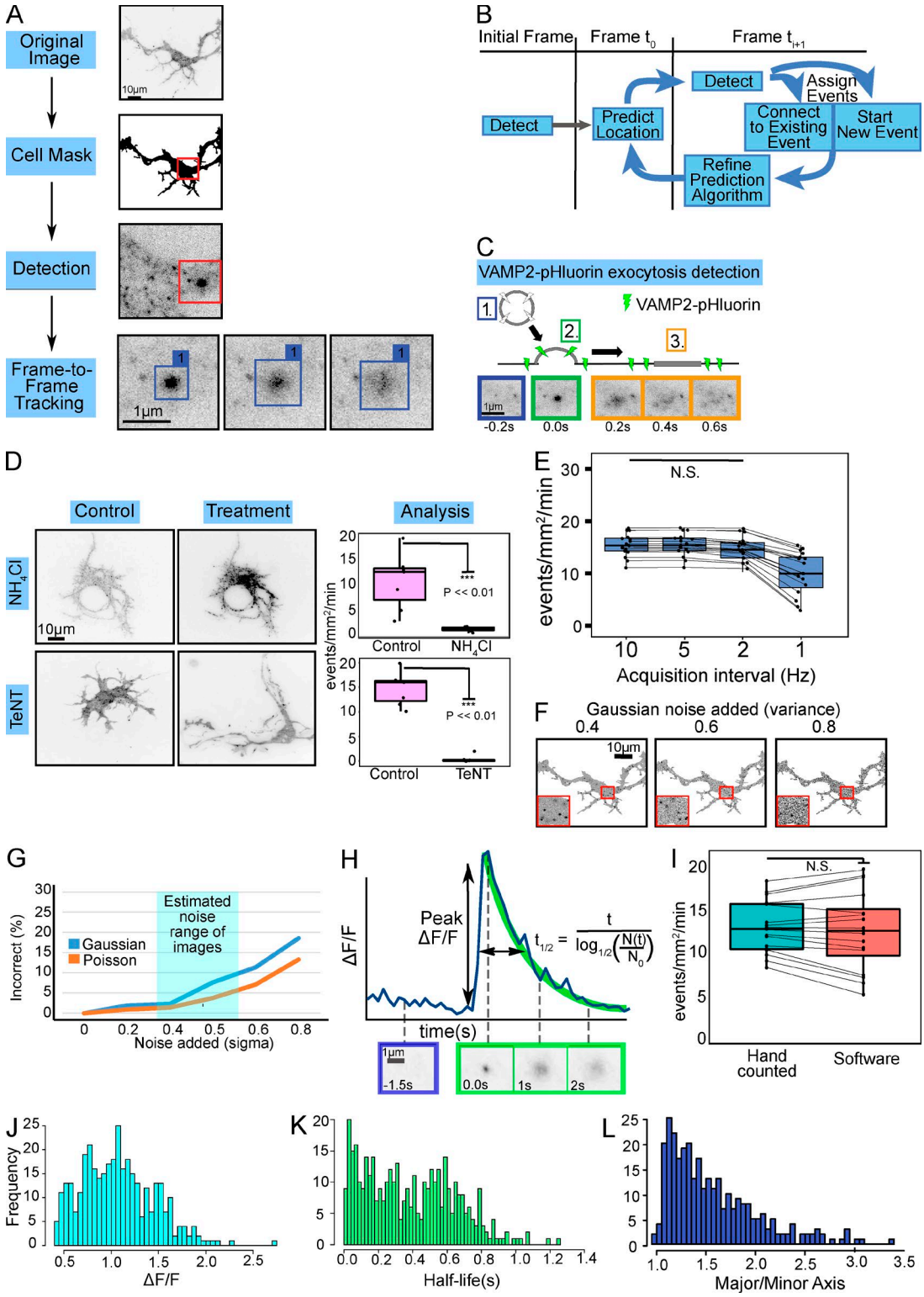

Figure 1. **Automated identification and analysis of VAMP-pHluorin mediated exocytosis. (A)** Overview of automated software. A cell mask is generated, followed by fluorescent maxima detection. A tracking matrix connects candidate events over time (Frame-to-Frame Tracking). **(B)** The tracking matrix was constructed using a Kalman filter to link a single exocytic event into a track over multiple frames. **(C)** Schematic and TIRF image montage show a typical exocytic event. Prefusion, VAMP2-pHluorin is not fluorescent (1, blue). Upon fusion pore opening (2, green), a bright fluorescent diffraction-limited spot appears. The VAMP2-pHluorin diffuses in the membrane over time (3, orange). **(D)** Example minimum projections of inverted TIRF time-lapse images before or after treatment with NH_4Cl or TeNT. NH_4Cl or TeNT treatment reduced the number of events detected (box plot, median ± interquartile range (IQR); whiskers reach minimum and maximum values within 1.5 times the IQR; $n = 6$ neurons per condition). See Video 2. **(E)** Box and whisker plots of effect of acquisition rate on exocytic detection ($n = 17$). **(F)** Examples of simulated images with noise of increasing Gaussian intensity. **(G)** Six simulations of exocytic events with increasing Gaussian or Poisson intensity demonstrate the robustness of the algorithm to image background and system noise. Typical experimental signal-to-background is highlighted in cyan. **(H)** ΔF/F for an individual exocytic event. Fusion pore opening occurs at time = 0 s. The normalized peak

Confirmation of detection of VAMP7-mediated exocytosis

We next tested whether the algorithm also accurately detected VAMP7-mediated events. Surprisingly, the frequency of VAMP7-mediated exocytosis detected was considerably lower than we previously reported using manual analysis (~15-fold less; Fig. S1 B; Winkle et al., 2014). Alkalization with NH_4Cl revealed numerous VAMP7-containing vesicles and confirmed VAMP7-pHluorin fluorescence was quenched by low pH (Fig. S3 A). To ensure the algorithm was capable of detecting VAMP7-mediated fusion, we coexpressed VAMP7-pHluorin along with an activating VAMP7 mutant lacking the autoinhibitory longin domain (VAMP7ΔLD; Martinez-Arca et al., 2000). VAMP7ΔLD expression increased the frequency of VAMP7-mediated exocytosis (Fig. S3 B), as previously shown (Burgo et al., 2013), demonstrating the algorithm was capable of detecting VAMP7-mediated events.

Several potential factors could account for the disparity between the algorithm and hand-counted VAMP7-mediated exocytosis, including different image acquisition rates, unique attributes of VAMP7-containing vesicles, and the more rigorous definition of a fusion event used by the algorithm. Artificially decreasing the temporal resolution of images to match the 2-Hz sampling rate used previously (Winkle et al., 2014) increased apparent exocytic frequency (Fig. S3 C) but did not account for the differences between automated and manually defined values. Because these newly identified events met algorithm requirements only at reduced temporal resolution, we conclude they were unlikely true events. The peak ΔF/F and $t_{1/2}$ were not significantly different between VAMP2-pHluorin and VAMP7-pHluorin (Fig. S3 D), indicating these were not the sources of incongruence. Along with artificially lowering the sampling rate, relaxing the algorithm requirement that events be nonmotile, a parameter that was difficult to assess manually, permitted the software to capture an exocytic frequency indistinguishable from previous studies (Fig. S3 C; Winkle et al., 2014). The mean squared displacement of events detected under this relaxed requirement was higher for VAMP7 than VAMP2 (Fig. S3 E), explaining why VAMP7-mediated events were previously overestimated and VAMP2-mediated events were not. To examine whether motile fluorescent puncta represented actual exocytic events, we coexpressed the autoinhibitory longin domain (VAMP7-LD; Martinez-Arca et al., 2000) with VAMP7-pHluorin. As reported, VAMP7-LD expression decreased VAMP7-pHluorin–mediated exocytic events when the nonmotile requirement was included in the detection algorithm (Fig. S3 B). Upon relaxation of this parameter, an increase in motile, VAMP7-mediated events was detected (Fig. S3, B and E). Together these results suggest that motile fluorescent events are not true exocytic events, and that the algorithm accurately detects exocytosis.

Spatiotemporal changes in exocytosis occur during development

With the algorithm validated, we set out to investigate developmental exocytosis. Dissociated neurons initially exhibit a "pancake-like" shape with peripheral protrusions. By 24 h in vitro, protrusions coalesce into immature neurites. By 48 h, neurons typically have several defined neurites, one of which is significantly longer and considered the axon. By 72 h, neurons are characterized by longer neurites and a longer, potentially branched axon. We hypothesized the temporal and spatial distribution of exocytosis in neurons would change over developmental time, and potentially involve fusion of both VAMP2- and VAMP7-containing vesicles. We measured VAMP2-pHluorin and VAMP7-pHluorin exocytic parameters in mouse embryonic day 15.5 (E15.5) cortical neurons after 24, 48, and 72 h in vitro (Fig. 2, A–I; and Videos 3 and 4). The rate of VAMP7-mediated exocytosis was negligible under these conditions (Fig. 2 E), so we focused on VAMP2-mediated exocytosis. We mapped the spatial occurrence and density of VAMP2-pHluorin–mediated events (Fig. 2 A), which suggested that their spatial distribution was not uniform. Neurons were segmented into soma and neurite regions of interest, and the frequencies of VAMP2-mediated exocytosis were compared, controlling for basal cell surface area (Fig. 2, B–D). At 24 h, exocytic frequency was faster compared with 48 and 72 h (Fig. 2 B), and faster in the soma compared with neurites (Fig. 2, C and D). This relationship between exocytic frequency in soma and neurites remained between 24 and 48 h (Fig. 2, C and D). However, at 72 h, a redistribution occurred, with an increased frequency of events in neurites and decreased frequency in the soma (Fig. 2, C and D).

Exocytic heat maps revealed that events were potentially clustered into spatial hot spots (Fig. 2 A). To determine if exocytosis was organized nonrandomly and to distinguish between clustering, randomness, or regular spacing (dispersal) of exocytic events, we adapted Ripley's K function (Ripley, 1976; see Materials and methods; Fig. 2, F and G). There has been limited use of the K function for analysis of exocytosis, restricted to individual cells of simple morphology (Díaz et al., 2010; Yuan et al., 2015). Group comparisons have not been performed, which limits statistical power, comparisons, and conclusions. In our case, an aggregated Ripley's K function (L[r]) compares the experimental distances in space or time between detected events in multiple cells (Fig. 2 F) against the theoretical distances between the same number of events if they occurred randomly in the same space or time. Simulated random events were performed for each test group, based on the experimental events and experimental space or time. When the experimental Ripley's K function ± SEM ($L_{Obs}[r]$) and the theoretical random Ripley's K function ($L_{theo}[r]$; Fig. 2 G, red line) overlap, events were randomly organized. At distances where $L_{Obs}(r)$ rose above $L_{theo}(r)$, exocytosis was clustered ($P < 0.05$), and at distances where $L_{Obs}(r)$ fell below $L_{theo}(r)$, events were dispersed ($P < 0.05$). At 24 h, exocytosis exhibited spatial randomness in soma and neurites as well as temporal randomness (Fig. 2, H and I). In contrast, at 48 and 72 h, exocytosis was clustered into spatial hot spots in both neurites and soma (Fig. 2 H), with higher clustering in the soma ($P < 0.05$). Spatial clustering in each region did not change between 48 and 72 h ($P > 0.05$). However, exocytosis became clustered into temporal bursts at these time points. Thus, spatial and temporal organization of exocytosis

change in fluorescence intensity (peak ΔF/F) and event $t_{1/2}$ (in s) are indicated. Initial fluorescence is estimated from 10 frames (1 s) before peak of fluorescence (initiation of exocytosis). $t_{1/2}$ is estimated using a negative exponential decay. **(I)** Box and whisker plots of user-based and automated detection of the frequency of VAMP2-pHluorin–mediated exocytosis were not different ($n = 16$, paired t test, $P = 0.56$). Data points represent frequency per cell. Histograms of measured peak ΔF/F (J), event $t_{1/2}$ (K), and major/minor axis of the first frame of each detected exocytic event (L). $n = 462$ exocytic events for each.

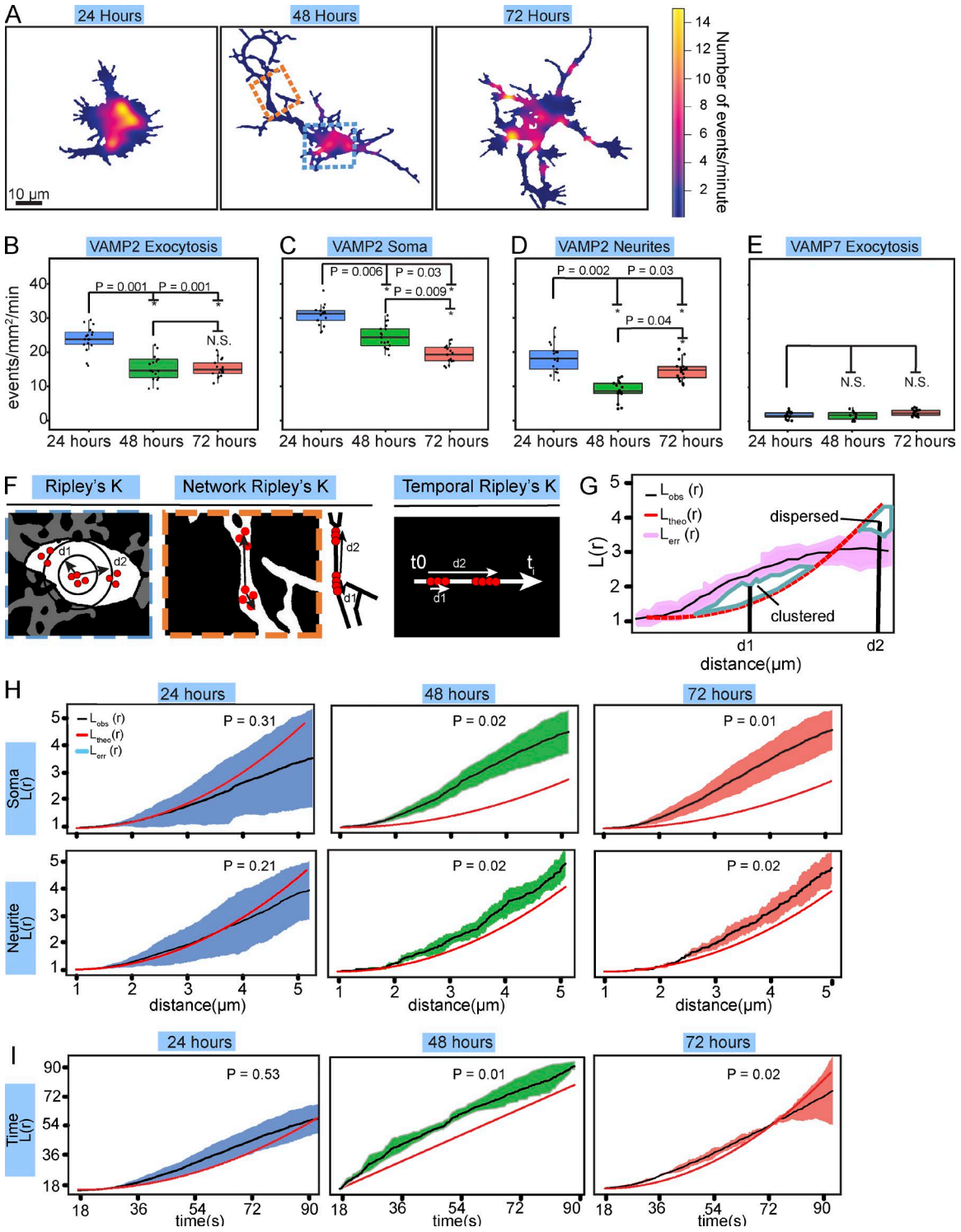

Figure 2. **Spatiotemporal changes in exocytosis during neuronal development. (A)** Heat maps of the density of VAMP2-mediated exocytosis in cortical neurons cultured in vitro for 24, 48, or 72 h before imaging. The blue and orange boxes demarcate soma and neurite examples used in F, respectively. **(B)** Frequency of VAMP2-pHluorin mediated exocytosis for basal plasma membrane of cortical neurons over developmental time. (*, $P < 0.05$; $n = 17$ cells per condition and 464, 455, and 466 exocytic events per condition; box and whiskers plots, box shows median ± IQR and whiskers reach minimum and maximum values within 1.5 times the IQR). See Video 3. **(C and D)** Box and whiskers plots of frequency of VAMP2-pHluorin–mediated exocytosis in the soma (C) and neurites (D) of cortical neurons. **(E)** Box and whiskers plots of frequency of VAMP7-pHluorin–mediated exocytosis for basal plasma membrane was not significantly different between time points ($n = 14$ cells per condition). See Video 4. **(F)** Schematics of Ripley's L(r) function in spatial and temporal dimensions. Red dots represent exocytic events. **(G)** Example of Ripley's L(r) analyses. The mean L(r) value of the aggregated data from multiple replicates ($L_{Obs}[r]$, black line) and standard error of the data ($L_{err}[r]$, pink) is compared with the expected L(r) value of completely random exocytic events ($L_{theo}[r]$, red dashed line). **(H)** Spatial Ripley's L(r) function analysis revealed that events were randomly distributed in the soma at 24 h, whereas exocytosis occurred in spatial clusters in the soma at 48 and 72 h. Exocytosis followed a similar pattern in the neurites ($L_{Obs}[r]$ = mean of 17 per condition). **(I)** Temporal Ripley's L(r) function of exocytic events over time in mouse cortical neurons, yet temporal bursts of exocytosis at 48 and 72 h in vitro ($L_{Obs}[r]$ = mean of 17 per condition). See Video 3.

evolved from random to clustered during neuronal morphogenesis and was distinct in the soma and neurites.

A mathematical approximation of membrane expansion

To determine the significance of VAMP2-mediated exocytosis in the expansion of neuronal surface area, we sought to calculate plasma membrane expansion and exocytic addition of membrane. A similar basal neuronal surface area was estimated from TIRF images of VAMP2-pHluorin and CAAX-GFP (Fig. S4 A). Folding of the plasma membrane was not observed in neurons expressing CAAX-GFP or VAMP2-pHluorin, whereas plasma membrane folding was apparent in nonneuronal cells in the culture expressing CAAX-GFP (Fig. S4 B). Scanning electron microscopy revealed that the apical membrane of neurites was flat, and only minimal apical membrane ruffling occurred on the growth cone and soma (Fig. S4 C). The neurite surface area was thus approximated by doubling the basal area. To account for the 3D shape of the soma with a flat basal surface attached to the coverslip, the soma was fit to a truncated ellipsoid. The height of the ellipsoid was approximated via confocal z-stacks (Fig. S4 D) and the length and width via the longest and shorted axes of the soma (Fig. S4 E). Neurite and soma surface areas were summated to estimate neuronal surface area. We derived the increase in cell surface area between 24 and 48 h using a Bayesian linear model, based upon empirical neuronal surfaces area measurements, using time in vitro as a categorical predictor (Fig. 3 A; see Materials and methods). Posterior predictive checking indicated that the model was a good fit (Fig. 3 B), with predicted credible regression lines showing a positive increase in surface area at 24 and 48 h (Fig. 3 C). The 90% confidence interval showed that the surface area increased by 979–1018 μm^2 with a mean of 999 μm^2 (Fig. 3 D, blue line). This amounted to a ∼57% increase over a 24-h time period, more than previous estimates (Pfenninger, 2009).

We estimated the surface area added by VAMP2-mediated exocytosis using the frequency of exocytosis (Fig. 2 B) and surface area of vesicles. A potential range of vesicular surface areas was approximated from vesicle diameters measured from transmission electron micrographs of cortical neurons at 48 h in vitro, with the assumption that vesicles were spherical (Fig. 3 E). Assuming a single population of vesicles with unimodal size distribution, and correcting for capturing random slices smaller than the actual vesicle diameter, we took the conservative estimate that the 75th percentile of the interquartile range represented the vesicle diameter (130 nm; Plooster et al., 2017). We also considered a smaller vesicle population, using the 25th percentile of the interquartile range (80 nm). We estimated membrane addition between 24 and 48 h in vitro, using the following formula:

$$y = \left\{ \begin{bmatrix} y_{upper} = S + (f_{24} \times z) \\ y_{lower} = S + (f_{48} \times z) \end{bmatrix} \right.,$$

where y represents predicted neuronal surface area at 48 h, S is neuronal surface area at 24 h, f_{24} and f_{48} are exocytic frequency at 24 and 48 h, respectively, and z is surface area of vesicles. Because the frequency of exocytosis was not measurably different on basal and apical membranes (Fig. S1), we used the mean frequency of basal exocytosis at 24 and 48 h (Fig. 2 B) to define the upper and lower bounds of VAMP2-mediated addition. The predicted mean membrane addition was ∼868–1,737 μm^2 using the smaller vesicle size, and ∼2,200–4,587 μm^2 using the larger vesicle size. These results suggested that VAMP2-mediated exocytosis provided excess material for developmental plasma membrane expansion (Fig. 3 D, green lines).

This excess delivery may be balanced by compensatory endocytosis. Both clathrin-mediated and clathrin-independent endocytosis occur at the synapse (Watanabe et al., 2013; Delvendahl et al., 2016), but the relative contributions of different forms of endocytosis at the synapse and in developing neurons is not known. In several cell types investigated, 95% of membrane internalization occurs through clathrin-mediated endocytosis (Pearse, 1976; Bitsikas et al., 2014). Therefore, we used tagRFP–clathrin light chain (Shaner et al., 2008) in conjunction with TIRF microscopy to measure the frequency of clathrin-mediated endocytosis (Fig. 3 F). The rate of endocytosis did not change between 24 and 48 h (Fig. 3 F). To exclude the clathrin coat, we measured the inner diameter of clathrin-coated vesicles from electron micrographs (34 nm; Fig. 3 G). With an additional parameter of clathrin-mediated membrane internalization, we updated our formula:

$$y = \left\{ \begin{bmatrix} y_{upper} = S + (f_{24} \times z) - (e_{24} \times x) \\ y_{lower} = S + (f_{48} \times z) - (e_{48} \times x) \end{bmatrix} \right.,$$

where e_{24} and e_{48} are the endocytic frequency at 24 and 48 h and x is the surface area of clathrin-coated vesicles.

The new predicted mean membrane addition between 24 and 48 h was ∼1–868 μm^2 using the smaller exocytic vesicle estimation, and ∼547–2416 μm^2 using the larger vesicle estimation (Fig. 3 D, orange lines). These results suggest that, by first approximation, plasma membrane expansion in cortical neurons can be explained by VAMP2-mediated exocytosis and clathrin-mediated endocytosis.

Netrin-1 modulates the spatiotemporal distribution of exocytic events in neurites

To further determine how exocytosis is organized during neuronal morphogenesis, we investigated the consequences of bath application of netrin-1 (Fig. 4, A–I), a guidance cue that accelerates neuronal morphogenesis (Winkle et al., 2016). Further validating the accuracy of the automated software, we confirmed previous findings (Winkle et al., 2014) that netrin stimulation increased the frequency of exocytosis (Fig. 4 E). Analysis of individual events identified parameters that were insensitive to netrin, including the major/minor axis of the vesicle fusion event, the peak ΔF/F, and the $t_{1/2}$ (Fig. 4, A–C). This suggests that netrin altered the probability of fusion, but the same vesicles fuse with the plasma membrane using similar mechanisms, as they contained indistinguishable amounts of VAMP2-pHluorin, and fluorescence dissipated with identical patterns.

Mapping the location and density of events (Fig. 4 D) revealed that netrin altered their nonuniform spatial distribution. Interestingly, netrin increased the frequency of exocytosis in the soma by ∼31% (Fig. 4 F), yet increased the frequency in neurites by 92% (Fig. 4 G), indicating neurites have increased responsiveness to netrin. Ripley's K function revealed that exocytic events were nonrandomly clustered at all distances in soma and neurites. In neurites, netrin enhanced clustering (Fig. 4 H). In contrast, spatial clustering in the soma appeared to relax after netrin addition, although these changes were not significant. Ripley's L(r) function showed temporal exocytic clustering that was lost upon netrin

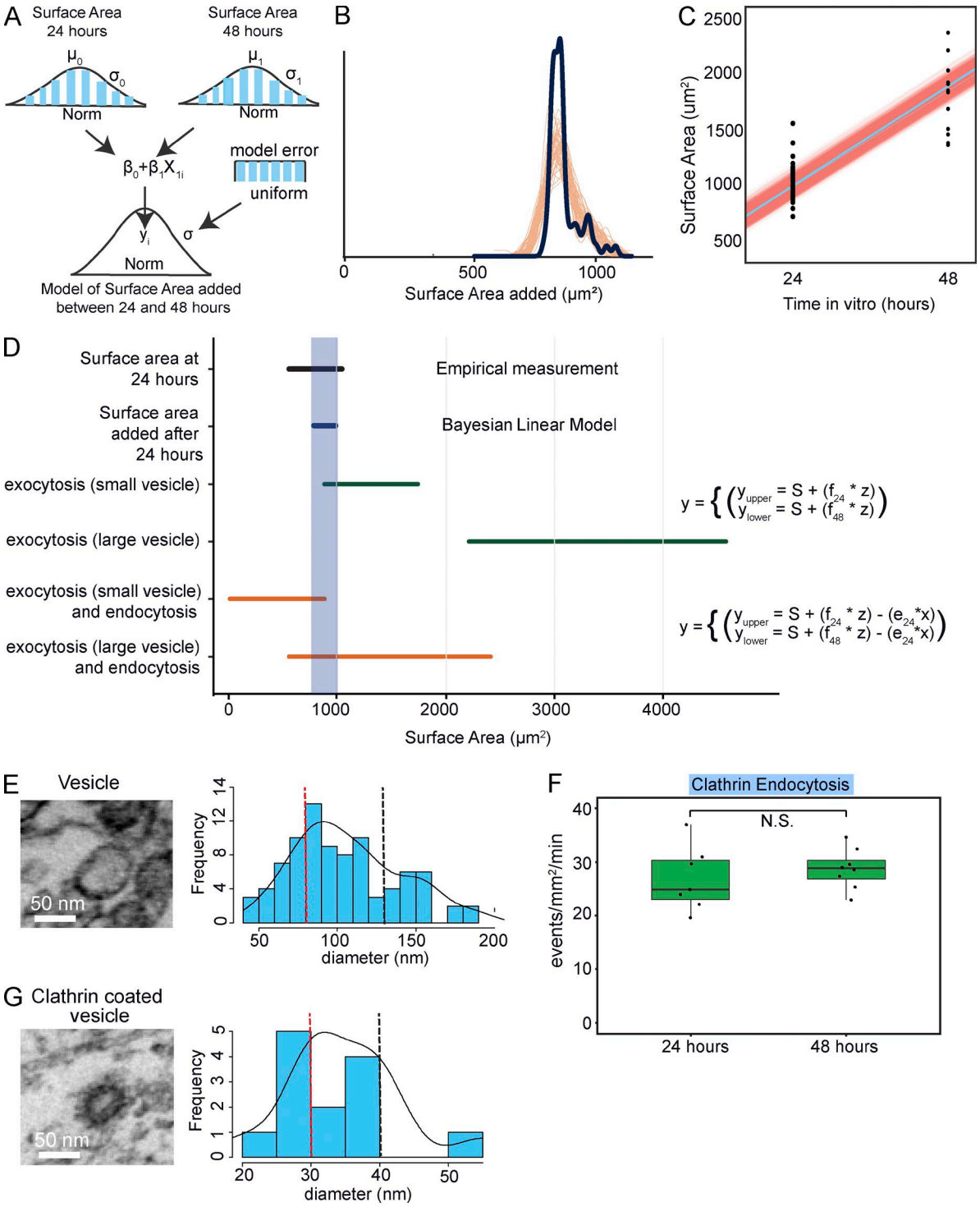

Figure 3. **A mathematical estimation of membrane expansion. (A)** Hierarchical diagram of the Bayesian linear model of neuronal surface area increases. Probability distributions (blue) of surface areas at 24 and 48 h represent priors imposed, with mean μ and SD σ for the normal distributions, and a uniform distribution for the model error. **(B)** Posterior predictions of surface area expansion by the model (orange lines) were compared with actual data (black line) to check for model fit. **(C)** Credible regression lines (orange) and mean (blue line) regression line of predicted plasma membrane expansion (n = 400 credible regression lines, n = 62 cells). **(D)** Estimates of membrane addition between 24 and 48 h. The black line is the measured surface area at 24 h in vitro. The blue line and blue shaded area represent predicted amount of plasma membrane expansion using a Bayesian linear model (A–C). Green lines represent predicted membrane added by VAMP2-mediated exocytosis. Orange lines represent predicted net membrane addition from VAMP2-mediated exocytosis after accounting for clathrin-mediated membrane removal. **(E)** Example transmission electron micrograph and histogram of measured diameters of non–clathrin-coated vesicles with density line overlaid (black solid line), 25th percentile (red dotted line), and 75th percentile (black dotted line) of the interquartile range (n = 88). **(F)** Box and whisker plots of frequency of clathrin-mediated endocytosis (n = 7 cells at 24 h and n = 8 cells at 24 h; box represents median ± IQR and whiskers reach minimum and maximum values within 1.5 times the IQR). **(G)** Example transmission electron micrograph and histogram of measured diameters of clathrin-coated vesicles with a density line overlaid (black solid line). The 25th percentile of the interquartile range (red dotted line, 30 nm) and 75th percentile of the interquartile range (black dotted vertical line, 40 nm; n = 13).

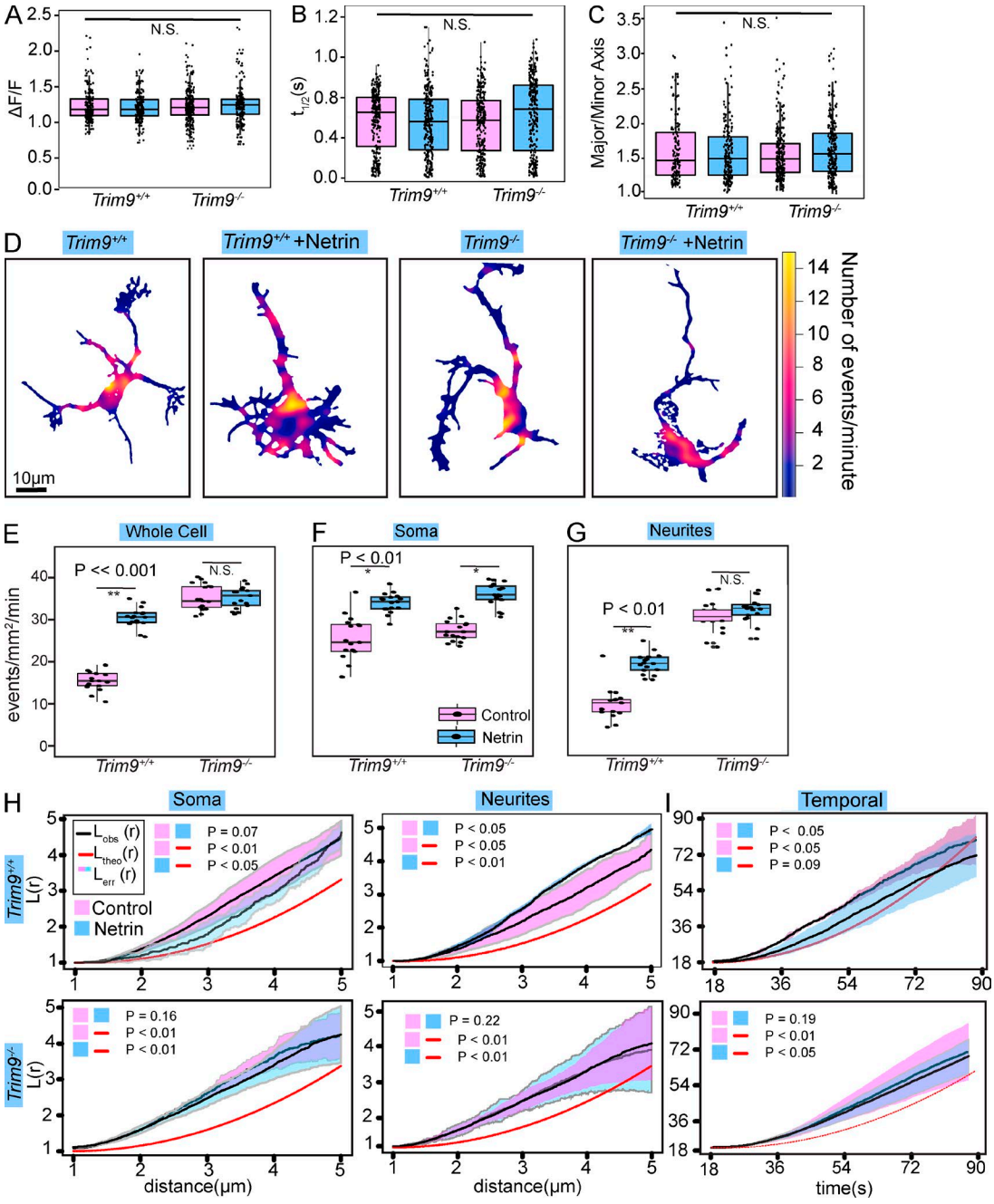

Figure 4. **Netrin and TRIM9-dependent changes in the distribution of exocytosis. (A–C)** Individual data points and box and whisker plots of peak ΔF/F (A), $t_{1/2}$ (B), and major/minor axis (C) of VAMP2-mediated exocytosis in *Trim9*$^{+/+}$ and *Trim9*$^{-/-}$ cortical neurons, treated or untreated with netrin-1 (n = 562, 632, 643, and 673 exocytic events per condition, respectively; box represents median ± IQR, whiskers reach minimum and maximum values within 1.5 times the IQR). **(D)** Heat maps of density of exocytosis. **(E)** Individual data points and box and whisker plots of frequency of VAMP2-pHluorin–mediated exocytosis (n = 17 cells per condition). **(F and G)** Frequency of VAMP2-pHluorin–mediated exocytic events in the soma (F) and neurites (G). **(H)** Ripley's L(r) function applied to the soma and neurites. The data line and pink surrounding SEM represent untreated, and the data line and surrounding blue SEM represent netrin-1–treated neurons (n = 17 cells per condition). **(I)** 1D Ripley's L(r) function of exocytic events over time (n = 17 cells per condition).

addition (Fig. 4 I). These results suggest that netrin modulates the distribution of exocytosis specifically in neurites and dissipates temporal clustering.

Tripartite motif 9 is required for netrin-dependent exocytic changes in neurites

To determine how netrin differentially affected exocytosis in the soma and neurites, we investigated the brain-enriched E3 ubiquitin ligase tripartite motif (TRIM) 9, implicated in constraint of exocytosis and netrin responses (Winkle et al., 2014). Genetic loss of *Trim9* did not change the major/minor axis of the initial vesicle fusion event, the peak ΔF/F, or the event $t_{1/2}$ (Fig. 4, A–C). Although *Trim9* deletion increased exocytic frequency and blocked netrin-dependent increases in exocytic frequency (Fig. 4 E), responses in the soma were similar to *Trim9*$^{+/+}$ neurons (Fig. 4 F), indicating somatic responses were TRIM9-independent. Neurites of *Trim9*$^{-/-}$ neurons, however, exhibited an approximately threefold increased frequency of basal exocytosis

that was not further increased by netrin (Fig. 4 G). This suggests that TRIM9 regulates VAMP2-mediated exocytosis in neurites.

Ripley's K function indicated that exocytic events were nonrandomly clustered at all distances measured in soma and neurites of *Trim9*$^{-/-}$ neurons (Fig. 4 H). Similar to *Trim9*$^{+/+}$ neurons, spatial clustering in the soma of *Trim9*$^{-/-}$ neurons appeared to relax after netrin addition. In contrast, spatial clustering in *Trim9*$^{-/-}$ neurites failed to increase in response to netrin (Fig. 4 H). Further, temporal clustering of exocytic events in *Trim9*$^{-/-}$ neurons persisted after netrin-1 addition (Fig. 4 I). This suggests that netrin-dependent modulation of the spatial distribution of exocytosis in neurites and the temporal clustering of exocytosis are TRIM9-dependent.

Different domains of TRIM9 modulate specific parameters of exocytosis in neurites

TRIM9 is a TRIM E3 ubiquitin ligase, characterized by a ubiquitin ligase RING domain, two BBox domains that modulate ligase activity, and a CC motif that mediates multimerization (Fig. 5 A). The TRIM9 CC motif also binds the exocytic t-SNARE SNAP25 (Li et al., 2001) and blocks SNARE complex formation and vesicle fusion (Winkle et al., 2014). The TRIM9 C-terminal SPRY domain binds the netrin receptor DCC (Winkle et al., 2014). To elucidate how these domains modified parameters of exocytosis and netrin response, we performed structure-function analysis. Expression of full-length and domain mutants of TRIM9 (Fig. 5 A) lacking the RING domain (TRIM9ΔRING), SPRY domain (TRIM9ΔSPRY), or CC motif (TRIM9ΔCC) in *Trim9*$^{-/-}$ neurons further indicated that TRIM9-dependent regulation of exocytosis occurred only in neurites (Fig. 5, B–D). Reintroduction of full-length TRIM9 reduced the elevated basal frequency of exocytosis and returned netrin sensitivity to exocytic frequency in neurites (Fig. 5 C), exocytic clustering in neurites (Fig. S5 A), and relaxation of temporal clustering (Fig. S5 B).

TRIM9ΔRING expression reduced elevated basal frequency of exocytosis in neurites, but failed to rescue netrin-dependent changes in exocytic frequency (Fig. 5 C), spatial clustering (Fig. S5 A), or temporal clustering (Fig. S5 B). This indicated the ligase domain was unnecessary to constrain exocytosis, but required for response to netrin. Although previous studies demonstrated that TRIM9-dependent ubiquitination altered substrate function (Menon et al., 2015; Plooster et al., 2017), we did not observe netrin-1 or TRIM9-dependent changes in the ubiquitination of SNAP25 (Fig. S5 C), suggesting that ubiquitin-dependent modulation of SNAP25 did not explain TRIM9-dependent changes in exocytosis. Expression of TRIM9ΔSPRY or TRIM9ΔCC failed to reduce the elevated frequency of exocytosis in the neurites ($P = 0.23$ and $P = 0.33$, respectively; Fig. 5 C) or the netrin-dependent reduction in temporal clustering (Fig. S5 B). Expression of TRIM9ΔSPRY, but not TRIM9ΔCC, rescued the spatial exocytic clustering in response to netrin-1 (Fig. S5 A), suggesting that TRIM9ΔSPRY retains partial netrin sensitivity. Together these results suggest that distinct domains of TRIM9 specifically constrain exocytosis and regulate spatial and temporal clustering in response to netrin.

Exocytosis in melanoma cells is distinctly organized

In contrast to developing neurons, nonneuronal interphase cells are typically at a steady-state size. To determine if spatial and temporal control of exocytosis varied in such a case, we investigated human VMM39 melanoma cells. We monitored exocytosis mediated by ubiquitous v-SNAREs by imaging VAMP3-pHluorin or VAMP7-pHluorin (Fig. 6 and Video 5). VAMP3-pHluorin and VAMP7-pHluorin exhibited no difference in the frequency of exocytosis (Fig. 6 A); however, this frequency was slower than mediated by VAMP2 and faster than

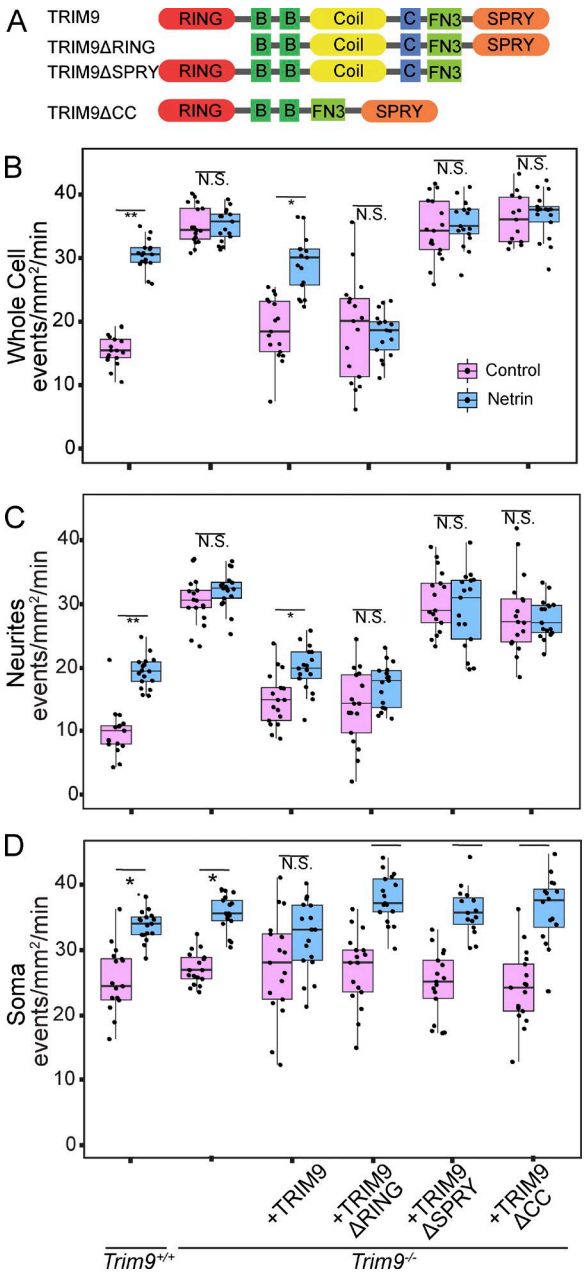

Figure 5. **Different domains of TRIM9 modulate specific parameters of exocytosis in neurites. (A)** Domain organization of mouse TRIM9 (top) and domain mutants that lack the ubiquitin ligase containing RING domain (TRIM9ΔRING), the DCC binding SPRY domain (TRIM9ΔSPRY), or the CC motif (TRIM9ΔCC), which mediates TRIM9 multimerization and interaction with SNAP25. **(B–D)** Box and whisker plots of frequency of VAMP2-pHluorin–mediated exocytosis across basal plasma membrane of neurons (box shows median ± IQR, whiskers reach minimum and maximum values within 1.5 times the IQR). (B), neurites (C), or soma (D) in *Trim9*$^{+/+}$ and *Trim9*$^{-/-}$ neurons expressing the indicated TRIM9 domain mutants ($n = 17$ for each condition; *, $P < 0.05$; **, $P < 0.005$). See Fig. S5.

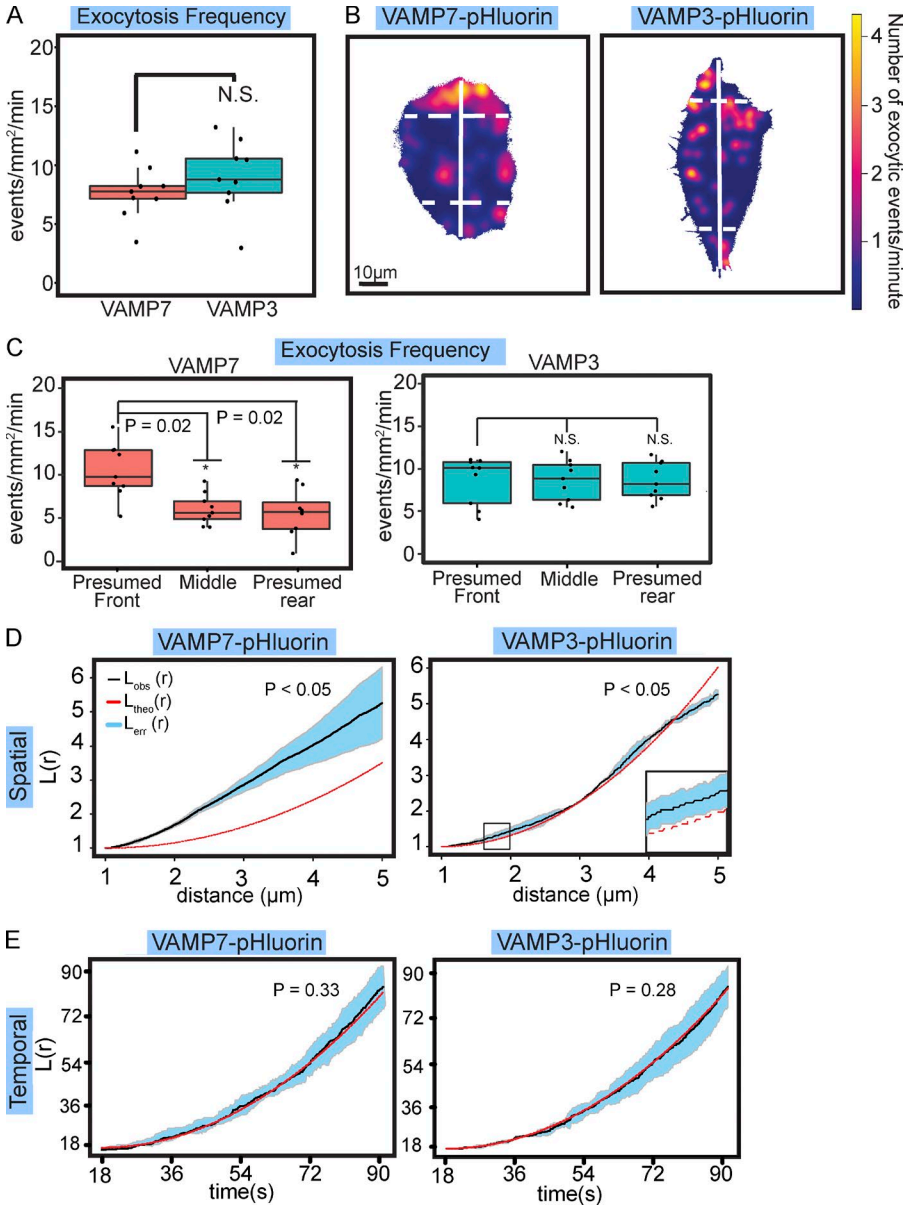

Figure 6. **Distinct spatiotemporal organization of fusion of different vesicles pools in melanoma cells. (A)** Box and whisker plots of frequency of VAMP7-pHluorin– and VAMP3-pHluorin–mediated exocytosis in VMM39 melanoma cells (n = 9 cells/condition; box shows median ± IQR, whiskers reach minimum and maximum values within 1.5 times the IQR). **(B)** Heat maps of density of VAMP7- and VAMP3-mediated exocytosis in representative VMM39 melanoma cells. Solid white line demarcates longest axis of the cell. Dashed perpendicular lines indicate minor axes 10 µm from the tips of the longest axis. The area encompassed from the edge of the cell to the dotted lines were measured to define a larger and smaller end of the cell. **(C)** Box and whiskers plots of number of exocytic events normalized to the larger end, middle, and smaller end of the cell. VAMP7-mediated exocytosis was polarized to the larger end of the cell (n = 9 cells). **(D)** 2D Ripley's L(r) function applied to the spatial occurrence of VAMP7- and VAMP3-mediated exocytic events (n = 9). VAMP7-mediated events exhibited nonrandom clustering at all distances measured, whereas VAMP3-mediated events were dispersed at larger distances in regularly spaced clusters 1.5–2.5 µm in size. **(E)** 1D Ripley's L(r) function applied to the temporal occurrence of VAMP7- and VAMP3-mediated exocytic events. Both VAMP7 and VAMP3-mediated events exhibited random temporal occurrence. See Video 5.

mediated by VAMP7 in neurons (P = 0.002 and P = 0.017, respectively). Mapping the location and density of VAMP3- and VAMP7-mediated events revealed their spatial distributions were distinct (Fig. 6 B). VAMP7-mediated events appeared polarized, whereas VAMP3-mediated events were distributed throughout the cell. To quantify this distribution, we segmented the cell with lines 10 µm from the edges of the cell, perpendicular to the longest axis (Fig. 6 B). VAMP7-mediated exocytosis occurred more in the larger end of the cell than in the middle and smaller end, whereas the frequency of VAMP3-mediated exocytosis was similar in each region (Fig. 6 C).

2D Ripley's L(r) analysis demonstrated that VAMP7-mediated events clustered at all distances measured (Fig. 6 D). VAMP3-mediated exocytosis was organized distinctly; exocytic clustering was observed at 1.5–2.5 µm (Fig. 6 D, inset). However, at larger distances (4.5 µm), the Ripley's L(r) value fell below spatial randomness, indicating dispersal of exocytic hot spots. 1D Ripley's L(r) analysis of the timing of VAMP3- and VAMP7-mediated exocytic events revealed that both were temporally random (Fig. 6 E). Together these investigations of the spatial and temporal organization of exocytosis in interphase cells revealed an organization and likely regulation of exocytosis distinct from developing neurons.

Discussion

Here we built a computer-vision image analysis tool and applied extended clustering statistics to demonstrate that the spatiotemporal distribution of constitutive VAMP2-mediated exocytosis is dynamic in developing neurons, modified by both developmental time and the guidance cue netrin-1, regulated differentially in the soma and neurites, and distinct from exocytosis in nonneuronal cells. To our knowledge, this represents the first systematic, automated investigation of exocytosis in developing neurons. Our algorithm has several advantages over previously reported detection algorithms (Sebastian et al., 2006; Díaz et al., 2010), including a more rigorous definition of an exocytic event, use of a Kalman filter for better tracking of events, and both simulated and experimental validation (Fig. 1 A and

Video 1). Although statistics for spatial clustering exist, they have not been applied in cells with extreme polarized morphology such as primary neurons, nor have they been aggregated to compare spatial and temporal parameters of fusion events across conditions. Our data and mathematical calculations suggest that in developing neurons, addition of membrane material by VAMP2-mediated exocytosis and endocytic retrieval of membrane by clathrin are sufficient to explain developmental plasma membrane expansion by first approximation.

Dynamic spatial regulation of exocytosis in developing neurons

Classic studies hypothesized that vesicles fuse at sites of cell growth (Feldman et al., 1981; Pfenninger and Friedman, 1993; Craig et al., 1995). Others suggested that membrane translocates anterogradely to the extending neurite tips (Popov et al., 1993), yet a systematic investigation of where vesicle fusion occurs has been lacking. We suggest that at earlier developmental stages, rapid membrane expansion is needed, but the localization of insertion is inconsequential. Perhaps with a less complex neuronal shape, cytoskeletal forces are sufficient to shape the plasma membrane. The developmental reduction in exocytic frequency but emergence of exocytic hot spots and shift of exocytosis toward neurites as neurons acquire a more complex morphology suggests that growth of individual neurites or individual branches requires local membrane insertion. Differences in the spatial distribution of exocytosis between developmental time points and cellular shapes suggest that the location and clustering of membrane insertion via exocytosis are regulated and developmentally critical to reach appropriate neuronal morphology. Our findings indicate that VAMP7-mediated vesicle fusion events were rare in the conditions and at the developmental time points investigated, and that VAMP2-mediated vesicle fusion occurred proximal to sites of growth, such as at the base of neurites and branches, supporting the anterograde membrane flow hypothesis at early developmental time points.

Calculating membrane growth in developing neurons

Several sources for membrane expansion have been identified, including exocytosis of secretory vesicles and/or lysosomes and membrane transfer at ER-plasma membrane contact sites (Arantes and Andrews, 2006; Pfenninger, 2009; Stefan et al., 2013). Additionally, astrocytes donate membrane material to neurons through lipoprotein particles (de Chaves et al., 1997; Mauch et al., 2001). The relative contributions of these sources have not been explored. Our results and calculations showed that the predicted surface area supplied by VAMP2-mediated exocytosis was roughly 2–10 times greater than the measured expansion of neuronal surface area, and further that clathrin-mediated endocytosis compensates by removing excess material. The measured increase in surface area most closely overlaps with vesicle membrane addition estimated by the addition of larger vesicles. This vesicle size is supported by the likely underestimation of vesicle diameter from electron micrographs and the unimodal distribution of vesicular VAMP2 content (Fig. 1 J). Although other modes of addition and retrieval may also be involved, VAMP2-mediated exocytosis and clathrin-mediated endocytosis together predict membrane addition that agrees with the membrane growth observed, suggesting that they may be the predominant mechanisms of membrane flux in developing neurons.

Exocytosis in the soma and neurites is distinctly regulated

Netrin-1 affects exocytosis distinctly in neurites and soma, suggesting there is regional regulation of exocytosis. Different proteins and vesicles have been shown to selectively enter certain regions of the developing neuron (Winckler et al., 1999; Dean et al., 2012; Petersen et al., 2014). We found that TRIM9 specifically regulated exocytosis in neurites; however, TRIM9 is also present in the soma. Whether specific TRIM9 isoforms localize and function distinctly or there is differential regulation of TRIM9 in the soma and neurites remains to be seen. In vitro, we found that cortical axons turn up attractive gradients of netrin-1 (Taylor et al., 2015) and that this is absent in *Trim9*$^{-/-}$ neurons (Menon et al., 2015). Whether a gradient of netrin-1 induces TRIM9-dependent asymmetrical changes in the spatiotemporal pattern of exocytosis in the growth cone that are required for axon turning is not known.

Unlike TRIM9, F-actin is distributed differently in the neurite and soma, as well as within the turning growth cone (He et al., 2010). Actin polymerization exerts a mechanical force on the plasma membrane, which increases tension and alters vesicle fusion (Kliesch et al., 2017). Because increased membrane tension has been coupled to increased exocytic activity (Wen et al., 2016), this may provide distinct regulation of exocytosis in the soma and neurites, and across the growth cone. Although a role for the actin cytoskeleton in exocytosis has been demonstrated in multiple cell types (Eitzen, 2003), a systematic investigation of this in developing neurons has not been performed.

Polarized exocytosis in nonneuronal migrating cells

The slower frequency of exocytosis in melanoma cells is consistent with melanoma cells not expanding their membrane. Polarized exocytosis has been suggested as a driving force in directional cell migration (Bretscher, 1996). Indeed, the rate of polarized exocytosis at the leading edge of fibroblasts correlates with the speed of migration, whereas disruption of cell polarization and polarized exocytosis is associated with loss of migration (Bergmann et al., 1983; Bretscher, 1996; Schmoranzer et al., 2003). The role of different VAMPs in migration has not been systematically explored, even though evidence exists of their heterogeneous distribution, transport, and cargo (Advani et al., 1998; Alberts et al., 2006; Oishi et al., 2006; Burgo et al., 2012; Bentley and Banker, 2015). The distinct spatial distributions of VAMP3- and VAMP7-mediated exocytosis observed here suggest unique roles for these two vesicle populations in melanoma cells, with polarized VAMP7-mediated exocytosis potentially associated with expansion of the leading edge during motility.

Materials and methods

Animal work

All mouse lines were on a C57BL/6J background and bred at the University of North Carolina at Chapel Hill with approval from the Institutional Animal Care and Use Committee. Mouse colonies were maintained in specific pathogen-free environment with 12-h light and dark cycles. Timed pregnant females were obtained by placing male and female mice together in a cage overnight; the following day was designated as E0.5 if the female had a vaginal plug. The generation of *Trim9*$^{-/-}$ mice is described in Winkle et al. (2014). Mice were genotyped using standard genotyping procedures.

Media, culture, and transfection of primary neurons and immortalized cell lines

Both male and female embryos were used to generate cultures and were randomly allocated to experimental groups. Cortical neuron cultures were prepared from day 15.5 embryos as previously described (Viesselmann et al., 2011). In brief, cortices were microdissected and neurons were dissociated with trypsin and plated on poly-D-lysine–coated glass-bottom culture dishes in neurobasal media supplemented with B27 (Invitrogen). This same media was used for all time-lapse experiments. For transfection, neurons were resuspended after dissociation in solution (Amaxa Nucleofector; Lonza) and electroporated with a nucleofector according to manufacturer protocol. Recombinant netrin was concentrated from the supernatant of HEK293 cells (Serafini et al., 1994). Neurons were stimulated with 500 ng/ml of netrin-1 added 1 h before imaging.

CRISPR-generated *TRIM9*$^{-/-}$ HEK293 cells were described previously (Menon et al., 2015). HEK293 and VMM39 cells were maintained in DMEM + glutamine supplemented with 10% FBS. For HEK293 and VMM39 cell transfections, HEK293 cells were transfected using Lipofectamine 2000 per manufacturer protocol.

Plasmids and antibodies

pEGFP-SNAP25B was acquired from L. Chamberlain (University of Edinburgh, Edinburgh, Scotland, UK). pcDNA3.1-HA rat DCC was acquired from M. Tessier-Lavigne (Stanford University, Stanford, CA). PcI-human-VAMP2-pHluorin was acquired from the Rothman laboratory (Yale University, New Haven, CT). pCAX-human VAMP3-pHluorin and pCAX-human VAMP7-pHluorin have a β-actin promoter (Gupton and Gertler, 2010). pEGFP-human VAMP7 N terminus (longin; aa 1–120) and VAMP7 C terminus were cloned into an mcherry vector. mTagRFP-T–clathrin-15 was obtained through Addgene from M. Davidson (Florida State University, Tallahassee, FL). FLAG-tagged ubiquitin was obtained from B. Philpot (University of North Carolina at Chapel Hill, Chapel Hill, NC). GFP-CAAX was obtained from Richard Cheney (University of North Carolina at Chapel Hill, Chapel Hill, NC). Antibodies include a rabbit polyclonal against GFP (A11122; Invitrogen) and ubiquitin (sc-8017; Santa Cruz Biotechnology).

Imaging and image analysis

All TIRF and widefield time-lapse imaging was performed using an inverted microscope (IX81-ZDC2; Olympus) with MetaMorph acquisition software (Molecular Devices), an electron-multiplying charge-coupled device (iXon), and a live cell imaging chamber (Tokai Hit Stage Top Incubator INUG2-FSX). The live cell imaging chamber maintained humidity, temperature at 37°C, and CO_2 at 5%. For all neuronal exocytosis assays, neurons in culture media expressing VAMP2-pHluorin or VAMP7-pHluorin were imaged at the indicated time point in vitro with a 100× 1.49 NA TIRF objective and a solid-state 491-nm laser illumination at 35% power at 110-nm penetration depth or in widefield epifluorescence using a xenon lamp. Images were acquired with MetaMorph software onto an iXon camera (Andor) using stream acquisition, imaging once every 100 ms for 2 min (10 Hz) or at the indicated acquisition rate. For measuring exocytosis in melanoma (VMM39) cell lines, images of interphase cells in culture media were acquired at 24 h after transfection with the indicated VAMP-pHluorin construct with a 100× 1.49 NA TIRF objective and a solid-state 491-nm laser illumination at 35% power at 110-nm penetration depth. Images were acquired with MetaMorph software onto an iXon every 500 ms for 3 min. For all endocytosis assays, neurons expressing clathrin light chain–tagRFP were imaged at 1 Hz with a 100× 1.49 NA TIRF objective and a solid-state 561-nm laser illumination at 40% power at 110-nm penetration depth.

Confocal Z-stack images of E15.5 cortical neurons at 2 d in vitro in culture media were acquired with Zeiss ZEN image acquisition software on an 880 confocal laser scanning microscope (Zeiss) with a 32-channel GaAsP spectral detector (Zeiss) with 45% quantum efficiency using a Plan Apo 63× 1.4 NA oil objective (Zeiss), equipped with an incubator ensuring temperature at 37°C and CO_2 at 5%. Scanning electron micrographs were acquired with a Zeiss Supra 25 Emission Scanning Electron Microscope with a Standard T-E secondary electron detector at 3,500× magnification, 5 Kv. Transmission electron micrographs were acquired with a FEI Tecnai T12 Transmission Electron Microscope using Tecnai software (Thermo Fisher Scientific) and a 1k × 1k digital CCD (model 794; Gatan).

ImageJ software (National Institutes of Health) was used for general viewing of images and videos.

Exocytic detection algorithm

The automated exocytic detection and image processing was written as a suite of MATLAB files with an execution script and performed in MATLAB, with analysis of Ripley's K and other statistics performed in the statistical language R with RStudio. To detect exocytic events, frames were first convolved with a Gaussian filter followed by local application of an h-dome transform (Vincent, 1993), to detect bright, round-shaped objects inside the cell mask against local variations in fluorescence. Gaussian mixed models were fit to local fluorescent maxima in each frame (Bishop, 2006), allowing the detection of both diffraction-limited and larger fluorescent objects. We defined a small radius expected to encompass the expansion and/or movement centered on potential fusion events identified in the initial frame (t_0). Using a cost matrix (Jaqaman et al., 2008), detected events that fell into the prediction radius were identified as the same object; if not, they were identified as a new object. The parameters of the cost matrix, including distance between predicted and detected locations, were determined experimentally based on the number of false positives and false negatives detected (Fig. S2, B and C; Matov et al., 2010). The prediction radius was refined in subsequent frames (t_i + 1) based on prior behavior of detected objects. This iterative process continued through the sequence of images to build connected object tracks, which represented potential exocytic events. Bona fide exocytic events were defined as transient, nonmotile (mean squared displacement <0.2 μm^2) objects that reached peak fluorescence intensity four deviations above the average local background intensity at t_0 (the first frame the object was detected in), followed by a detectable exponential fluorescent decay (≥3 frames) with no limit on how long the events could last. Objects that did not meet these requirements were discarded.

Clathrin-mediated endocytosis detection

An h-dome transform was performed on neurons expressing clathrin light chain–tagRFP to detect fluorescent maxima in each frame. Fluorescent puncta that lasted at least 20 s before disappearing were considered endocytic events (Loerke et al., 2009).

NH_4Cl and TeNT treatments

Neurons transfected with VAMP2-pHluorin or VAMP7-pHluorin were imaged at 48 h as in the Imaging and image analysis section. Either 25 mM NH_4Cl or 50 nM TeNT (Sigma-Aldrich) were added to the neurons followed by either immediate imaging for NH_4Cl treatment or imaging 30 min after the addition of TeNT. Analysis of exocytic events were performed as described in the Exocytic detection algorithm section.

Simulation of exocytosis

VAMP2-pHluorin signal on the cell surface was simulated with a normal distribution using a mean and SD equivalent to the measured median, to account for outlier fluorescent pixels, and SDs of experimental VAMP2-pHluorin signal. Gaussian fluorescent peaks with varying means and SDs, approximated from user-identified exocytic

events, were added to simulate exocytic events. To represent random noise, a range of intensities based on typical images that followed a Poisson or Gaussian distribution were added to simulated images (Pawley, 1990; Waters, 2009).

Surface area estimation

To estimate the surface area, we used TIRF images of VAMP2-pHluorin expressing cells. The soma was identified and segmented from the neurites, and the basal surface area of each was calculated separately. Total neurite area was estimated as doubling the measured basal membrane area. The mean height of the soma (~11 µm) was obtained from confocal image z-stacks through cortical neurons at 48 h in vitro. The major and minor axis of the soma were measured and used with the mean height of the soma to calculate the surface area using the calculation for a truncated ellipsoid:

$$\frac{3}{4}4\pi\left[\frac{(ab)^{1.6}+(ac)^{1.6}+(bc)^{1.6}}{3}\right]^{\frac{1}{1.6}}+\frac{\pi ab}{c^2}(0.75c)(3c-0.75c),$$

where a, b, and c represent the three axes of the soma (length, width, and height, respectively). The surface area of soma and neurites were summated to obtain the final surface area estimate of the neuron. For calculating local SD of fluorescence intensity of GFP-CAAX, a 9 × 9 square filter was convolved on each pixel, replacing the value with the SD of the 9 × 9 block of pixels.

Statistical analysis

The software package R was primarily used for statistical analysis of data. Both R and Adobe Illustrator were used for the generation of figures. At least three independent experiments were performed for each assay. Normality of data was determined by Shapiro-Wilk test. For two-sample comparisons of normally distributed data, an unpaired *t* test was used for two independent samples, or a paired *t* test for paired samples. For multiple comparisons, ANOVA was used to determine significance, followed by unpaired or paired *t* tests corrected using the Benjamini-Hochberg method. For analysis of nonnormally distributed data, the Mann-Whitney test was used for two samples. For more than two samples, Kruskal-Wallis nonparametric ANOVA was used to determine significance followed by the Benjamini-Hochberg method. For all Ripley's L(r) functions, comparisons between individual L(r) functions were made using the Studentized permutation test (Hahn, 2012). To test for differences between groups of L(r) functions, we first aggregated K functions and performed Diggle's test, (Diggle et al., 1991). The R package "brms" was used to run the Bayesian linear model and generate the graphs used in Fig. 3.

Bayesian linear model

A Bayesian linear model was used to calculate the increase in neuronal surface area between 24 and 48 h in vitro. We made the assumption that neuronal surface area can only increase over time, and thus used a Γ link function for the response variable. To give more weight to the data, we chose a weakly informative prior distribution for the predictor (normal distribution with mean of 500, σ of 100), with the assumption that neurons increased surface area over time with no chance of decreasing surface area, and a uniform distribution 0–10 for the variance.

Ripley's K test of complete spatial randomness or complete temporal randomness

Ripley's K function is defined in two dimensions as

$$\hat{\hat{K}}(r) = \lambda^{-1}\sum_{i\neq j} w\left(l_i,l_j\right)^{-1}\frac{I\left(d_{ij}<r\right)}{n},$$

where λ is the intensity, described as $\lambda = n/A$, A is the area encompassing the points, n is the number of points, I is an indicator function (1 if true and 0 if false), d_{ij} is the Euclidian distance between the ith and jth point, and r is the search radius. To correct for edge effects, the function is weighted by $w(l_i,l_j)$, which represents the fraction of search radius that contains A.

The soma of neurons was analyzed using Ripley's K function. However, long, narrow, and branched neurites posed a challenge to the spatial analysis, even with an edge corrector. Thus, we skeletonized neurites, and considered them a 1D network (Fig. 2 F). Exocytic events in neurites were mapped to the nearest point on the network. We then performed an extension of Ripley's K function, the network K function, which takes the form

$$\hat{\hat{K}}(r) = \frac{|L_t|}{(n-1)n}\sum_{i=1}^{n}\sum_{i\neq j,j=1}^{n} I\left(d_{ij}<t\right),$$

where L_t is the union of all links in the network, and d_{ij} is the network distance between points (Okabe and Yamada, 2001).

Finally, to test the temporal clustering of exocytosis, we performed Ripley's K function in 1D:

$$\hat{\hat{K}}(r) = \lambda^{-1}\sum_{i\neq j} w\left(l_i,l_j\right)^{-1}\frac{I\left(u_{ij}<r\right)}{n},$$

where u_{ij} is the distance between points on a 1D line ($u_{ij} = |u_i - u_j|$); $w(l_i,l_j)$ is the fraction of the search length, r, that overlaps the number line (0,T); and T is the length of the 1D search space (Fig. 2 F, total time imaged for temporal analysis).

With the assumption that all cells measured in a group exhibit the same clustering pattern, the group-specific mean function is defined as:

$$\bar{K}_i(r) = \sum_{j=1}^{m_i} w_{ij}\hat{\hat{K}}(t)$$

for each ith group, and the mean K function mean of the total population is

$$\bar{\bar{K}}(r) = \frac{1}{n}\sum_{i=1}^{g} n_i\bar{K}_i(t),$$

where $w_{ij} = n_{ij}/n_i$, n_i is the number of points in the ith group, and n is the total number of points of all groups. A test statistic

$$D_g = \sum_{i=1}^{g}\int_0^{t_0}\left[\bar{K}_i^{1/2}(t)-\bar{\bar{K}}^{1/2}(t)\right]^2 dt$$

is used to test differences between groups. We use the mean sampling variance of the functions weighted by w_{ij} to construct confidence intervals ± two SEMs. To attach p-values to observed test statistics, we use a bootstrapping procedure to determine the distribution of D_g. To do so, we define

$$\hat{\hat{R}}_{ij}(t) = n_{ij}^{1/2}\left[\hat{\hat{K}}_{ij}(t)-\hat{\hat{K}}_i(t)\right]$$

as the residual K functions. We obtain the approximate distribution of D_g by bootstrapping the residual K functions

$$\hat{\hat{K}}_{ij}^{*}(t) = \bar{\bar{K}}(t) + n_{ij}^{-1/2}\hat{\hat{R}}_{ij}^{*}(t)$$

drawing at random with replacement from $R_{ij}(t)$, keeping the group sizes fixed. This bootstrapping procedure is performed 999 times, and the observed D_g values are ranked among the bootstrapped D_g^* values to obtain p-values of the null hypothesis: that the two groups being compared came from the same distribution (Diggle et al., 1991).

For ease of interpretation, we use the variance-stabilized Ripley's K function, L(r), which gives an L(r) equivalent to the radius (r) under spatial or temporal randomness ($L_{theo}[r]$). To test whether

exocytic events are clustered, the L(r) function of aggregated observed data is compared with Monte Carlo simulations of complete spatial randomness ($L_{CSR}[r]$) or complete temporal randomness ($L_{CTR}[r]$; Diggle, 2013). Under traditional Ripley's K analysis, $L_{CSR}(r)$ is equivalent to πr^2; in the case of a network function, $L_{CSR}(r)$ is equivalent to the uniform distribution of points on the network. $L_{CTR}(r)$ is equivalent to a uniform distribution.

Ubiquitination assays

To measure ubiquitination of SNAP25, HEK293 cells were transfected with HA-DCC, FLAG-ubiquitin, and SNAP25-GFP and cultured for 24 h. 4 h before lysing, the cells were treated with 10 µM MG-132 or 10 µM MG-132 and 600 ng/ml of netrin-1. The treated HEK cells were lysed in 20 mM Tris-Cl, 250 mM NaCl, 3 mM EDTA, 3 mM EGTA, 0.5% NP-40, 1% SDS, 2 mM DTT, 5 mM *N*-ethylmaleimide, 3 mM iodoacetamide, and protease and phosphatase inhibitors (15 mM sodium pyrophosphate, 50 mM sodium fluoride, 40 mM β-glycophosphate, 1 µM sodium vanadate, 150 µg/ml phenylmethylsulfonyl fluoride, 1 µg/ml leupeptin, and 5 µg/ml aprotinin), pH, 7.4. For 6 million cells, 270 µl of lysis buffer was added and incubated on ice for 10 min. Cells were removed from the dish and transferred into tubes. 30 µl of 1× PBS was added, and samples were gently vortexed. Samples were boiled immediately for 20 min until they turned clear, then were centrifuged at 14,000 *g* for 10 min. The boiled samples were diluted using lysis buffer without SDS to reduce the SDS concentration to 0.1%. For immunoprecipitation of GFP-SNAP25, IgG-conjugated A/G beads (sc-2343; Santa Cruz Biotechnology) were used to preclear lysates for 1.5 h at 4°C with agitation. A/G beads coupled to anti-GFP Ab (Neuromab) were agitated within precleared lysates overnight at 4°C to precipitate GFP-SNAP25. Beads were washed three times with lysis buffer, and bound proteins were resolved by SDS-PAGE and analyzed by immunoblotting for GFP, FLAG, and HA.

Online supplemental material

Fig. S1 shows that TIRF imaging captures VAMP2-pHluorin– and VAMP7-pHluorin–mediated exocytosis efficiently. Fig. S2 presents the Kalman filter algorithm and parameter selection. Fig. S3 presents confirmation of VAMP7-pHluorin exocytosis. Fig. S4 presents estimation of exocytic addition and membrane surface area increases in developing neurons. Fig. S5 shows that specific domains of TRIM9 modulate distinct parameters of exocytosis in neurites. Video 1 shows algorithm identification of exocytic events. Video 2 confirms that detected exocytic events are transient and TeNT-sensitive. Video 3 demonstrates that VAMP2-mediated exocytosis changes over developmental time. Video 4 shows that VAMP7-mediated exocytosis adds a negligible amount of membrane. Video 5 demonstrates VAMP3- and VAMP7-mediated exocytosis in VMM39 melanoma cells. Run_script.m runs the entire detection algorithm over a folder of image stacks. Cell_mask.m creates a binary mask of a cell from a fluorescent image. Detection_algorithm.m finds all possible exocytic events and fluorescent puncta in each image of a z-stack. Multiobject_tracking.m performs the Kalman filter function, linking fluorescent events across frames and throwing out nonexocytic objects. Extract_fusion.m compiles the fluorescent pixel values, time points, and x and y positions of exocytic events and saves them to a CSV file. Full_fusion_script.R computes features of each exocytic event. Cell_SurfaceArea.R computes the surface area of the cell soma gives the length, width, and height. Bayesian_Cell_Model.R performs linear Bayesian analysis. Spatial_analysis.R performs the Ripley's K function on exocytosis given a list of events and a cell mask.

Acknowledgments

We thank Patrick Brennwald and the Gupton laboratory for thoughtful critiques. We thank Caroline Monkiewicz, Charles Park, Divya Mahesh, and Emily Wolfgram for contributions and technical support. We thank Melissa Plooster for confocal microscopy measurements of soma height and Nick Boyer for SEM images. We thank the Computational Image Analysis course at the Marine Biological Laboratory at Woods Hole for providing the foundation and expertise for building the image analysis software. We thank the Initiative for Maximizing Student Diversity for their continued support.

This work was supported by National Institutes of Health grants GM108970 to S.L. Gupton and NS103586 to F.L. Urbina.

The authors declare no competing financial interests.

Author contributions: F.L. Urbina designed and performed experiments, analyzed data, and wrote the paper. S.M. Gomez consulted regarding framework of automated detection and analysis and edited the manuscript. S.L. Gupton designed experiments, provided guidance in software design, and wrote the paper.

Submitted: 13 September 2017
Revised: 17 November 2017
Accepted: 14 December 2017

References

Aalto, M.K., H. Ronne, and S. Keränen. 1993. Yeast syntaxins Sso1p and Sso2p belong to a family of related membrane proteins that function in vesicular transport. *EMBO J.* 12:4095–4104.

Advani, R.J., H.R. Bae, J.B. Bock, D.S. Chao, Y.C. Doung, R. Prekeris, J.S. Yoo, and R.H. Scheller. 1998. Seven novel mammalian SNARE proteins localize to distinct membrane compartments. *J. Biol. Chem.* 273:10317–10324. https://doi.org/10.1074/jbc.273.17.10317

Alberts, P., R. Rudge, T. Irinopoulou, L. Danglot, C. Gauthier-Rouvière, and T. Galli. 2006. Cdc42 and actin control polarized expression of TI-VAMP vesicles to neuronal growth cones and their fusion with the plasma membrane. *Mol. Biol. Cell.* 17:1194–1203. https://doi.org/10.1091/mbc.E05-07-0643

Arantes, R.M.E., and N.W. Andrews. 2006. A role for synaptotagmin VII-regulated exocytosis of lysosomes in neurite outgrowth from primary sympathetic neurons. *J. Neurosci.* 26:4630–4637. https://doi.org/10.1523/JNEUROSCI.0009-06.2006

Bentley, M., and G. Banker. 2015. A Novel Assay to Identify the Trafficking Proteins that Bind to Specific Vesicle Populations. Curr. Protoc. Cell Biol. 69:13.8.1–13.8.12.

Bergmann, J.E., A. Kupfer, and S.J. Singer. 1983. Membrane insertion at the leading edge of motile fibroblasts. *Proc. Natl. Acad. Sci. USA.* 80:1367–1371. https://doi.org/10.1073/pnas.80.5.1367

Bishop, C.M. 2006. Mixture models and EM. In Pattern Recognition and Machine Learning. Springer Science+Business Media, LCC, New York. 423–455.

Bitsikas, V., I.R. Corrêa Jr., and B.J. Nichols. 2014. Clathrin-independent pathways do not contribute significantly to endocytic flux. *eLife.* 3:e03970.

Bloom, M., E. Evans, and O.G. Mouritsen. 1991. Physical properties of the fluid lipid-bilayer component of cell membranes: a perspective. *Q. Rev. Biophys.* 24:293–397. https://doi.org/10.1017/S0033583500003735

Brennwald, P., B. Kearns, K. Champion, S. Keränen, V. Bankaitis, and P. Novick. 1994. Sec9 is a SNAP-25-like component of a yeast SNARE complex that may be the effector of Sec4 function in exocytosis. *Cell.* 79:245–258. https://doi.org/10.1016/0092-8674(94)90194-5

Bretscher, M.S. 1996. Moving membrane up to the front of migrating cells. *Cell.* 85:465–467. https://doi.org/10.1016/S0092-8674(00)81246-5

Burgo, A., V. Proux-Gillardeaux, E. Sotirakis, P. Bun, A. Casano, A. Verraes, R.K.H. Liem, E. Formstecher, M. Coppey-Moisan, and T. Galli. 2012. A molecular network for the transport of the TI-VAMP/VAMP7 vesicles from cell center to periphery. *Dev. Cell.* 23:166–180. https://doi.org/10.1016/j.devcel.2012.04.019

Burgo, A., A.M. Casano, A. Kuster, S.T. Arold, G. Wang, S. Nola, A. Verraes, F. Dingli, D. Loew, and T. Galli. 2013. Increased activity of the vesicular soluble N-ethylmaleimide-sensitive factor attachment protein receptor TI-VAMP/VAMP7 by tyrosine phosphorylation in the Longin domain.

J. Biol. Chem. 288:11960–11972. https://doi.org/10.1074/jbc.M112.415075

Craig, A.M., R.J. Wyborski, and G. Banker. 1995. Preferential addition of newly synthesized membrane protein at axonal growth cones. *Nature.* 375:592–594. https://doi.org/10.1038/375592a0

Dean, C., H. Liu, T. Staudt, M.A. Stahlberg, S. Vingill, J. Bückers, D. Kamin, J. Engelhardt, M.B. Jackson, S.W. Hell, and E.R. Chapman. 2012. Distinct subsets of Syt-IV/BDNF vesicles are sorted to axons versus dendrites and recruited to synapses by activity. *J. Neurosci.* 32:5398–5413. https://doi.org/10.1523/JNEUROSCI.4515-11.2012

de Chaves, E.I., A.E. Rusiñol, D.E. Vance, R.B. Campenot, and J.E. Vance. 1997. Role of lipoproteins in the delivery of lipids to axons during axonal regeneration. *J. Biol. Chem.* 272:30766–30773. https://doi.org/10.1074/jbc.272.49.30766

Delvendahl, I., N.P. Vyleta, H. von Gersdorff, and S. Hallermann. 2016. Fast, Temperature-Sensitive and Clathrin-Independent Endocytosis at Central Synapses. *Neuron.* 90:492–498. https://doi.org/10.1016/j.neuron.2016.03.013

Díaz, E., G. Ayala, M.E. Díaz, L.-W. Gong, and D. Toomre. 2010. Automatic detection of large dense-core vesicles in secretory cells and statistical analysis of their intracellular distribution. *IEEE/ACM Trans. Comput. Biol. Bioinform.* 7:2–11. https://doi.org/10.1109/TCBB.2008.30

Diggle, P.J. 2013. Statistical Analysis of Spatial and Spatio-Temporal Point Patterns. Third edition. Oxford University Press, New York.

Diggle, P.J., N. Lange, and F.M. Benes. 1991. Analysis of Variance for Replicated Spatial Point Patterns in Clinical Neuroanatomy. *J. Am. Stat. Assoc.* 86:618–625. https://doi.org/10.1080/01621459.1991.10475087

Eitzen, G. 2003. Actin remodeling to facilitate membrane fusion. *Biochim. Biophys. Acta.* 1641:175–181. https://doi.org/10.1016/S0167-4889(03)00087-9

Engle, E.C.2010. Human Genetic Disorders of Axon Guidance. Cold Spring Harb. Perspect. Biol.2:a001784.

Feldman, E.L., D. Axelrod, M. Schwartz, A.M. Heacock, and B.W. Agranoff. 1981. Studies on the localization of newly added membrane in growing neurites. *J. Neurobiol.* 12:591–598. https://doi.org/10.1002/neu.480120607

Galli, T., A. Zahraoui, V.V. Vaidyanathan, G. Raposo, J.M. Tian, M. Karin, H. Niemann, and D. Louvard. 1998. A novel tetanus neurotoxin-insensitive vesicle-associated membrane protein in SNARE complexes of the apical plasma membrane of epithelial cells. *Mol. Biol. Cell.* 9:1437–1448. https://doi.org/10.1091/mbc.9.6.1437

Gupton, S.L., and F.B. Gertler. 2010. Integrin signaling switches the cytoskeletal and exocytic machinery that drives neuritogenesis. *Dev. Cell.* 18:725–736. https://doi.org/10.1016/j.devcel.2010.02.017

Hahn, U. 2012. A Studentized Permutation Test for the Comparison of Spatial Point Patterns. *J. Am. Stat. Assoc.* 107:754–764. https://doi.org/10.1080/01621459.2012.688463

He, M., Z.-H. Zhang, C.-B. Guan, D. Xia, and X.-B. Yuan. 2010. Leading tip drives soma translocation via forward F-actin flow during neuronal migration. *J. Neurosci.* 30:10885–10898. https://doi.org/10.1523/JNEUROSCI.0240-10.2010

Heuser, J.E., and T.S. Reese. 1973. Evidence for recycling of synaptic vesicle membrane during transmitter release at the frog neuromuscular junction. *J. Cell Biol.* 57:315–344. https://doi.org/10.1083/jcb.57.2.315

Jaqaman, K., D. Loerke, M. Mettlen, H. Kuwata, S. Grinstein, S.L. Schmid, and G. Danuser. 2008. Robust single-particle tracking in live-cell time-lapse sequences. *Nat. Methods.* 5:695–702. https://doi.org/10.1038/nmeth.1237

Kalman, R.E. 1960. A New Approach to Linear Filtering and Prediction Problems. *Int. J. Eng. Trans. A.* 82:35.

Kliesch, T.-T., J. Dietz, L. Turco, P. Halder, E. Polo, M. Tarantola, R. Jahn, and A. Janshoff. 2017. Membrane tension increases fusion efficiency of model membranes in the presence of SNAREs. *Sci. Rep.* 7:12070. https://doi.org/10.1038/s41598-017-12348-w

Li, Y., L.-S. Chin, C. Weigel, and L. Li. 2001. Spring, a novel RING finger protein that regulates synaptic vesicle exocytosis. *J. Biol. Chem.* 276:40824–40833. https://doi.org/10.1074/jbc.M106141200

Link, E., L. Edelmann, J.H. Chou, T. Binz, S. Yamasaki, U. Eisel, M. Baumert, T.C. Südhof, H. Niemann, and R. Jahn. 1992. Tetanus toxin action: inhibition of neurotransmitter release linked to synaptobrevin proteolysis. *Biochem. Biophys. Res. Commun.* 189:1017–1023. https://doi.org/10.1016/0006-291X(92)92305-H

Loerke, D., M. Mettlen, D. Yarar, K. Jaqaman, H. Jaqaman, G. Danuser, and S.L. Schmid. 2009. Cargo and dynamin regulate clathrin-coated pit maturation. *PLoS Biol.* 7:e57. https://doi.org/10.1371/journal.pbio.1000057

Martinez-Arca, S., P. Alberts, A. Zahraoui, D. Louvard, and T. Galli. 2000. Role of tetanus neurotoxin insensitive vesicle-associated membrane protein (TI-VAMP) in vesicular transport mediating neurite outgrowth. *J. Cell Biol.* 149:889–900. https://doi.org/10.1083/jcb.149.4.889

Matov, A., K. Applegate, P. Kumar, C. Thoma, W. Krek, G. Danuser, and T. Wittmann. 2010. Analysis of microtubule dynamic instability using a plus-end growth marker. *Nat. Methods.* 7:761–768. https://doi.org/10.1038/nmeth.1493

Mauch, D.H., K. Nägler, S. Schumacher, C. Göritz, E.C. Müller, A. Otto, and F.W. Pfrieger. 2001. CNS synaptogenesis promoted by glia-derived cholesterol. *Science.* 294:1354–1357. https://doi.org/10.1126/science.294.5545.1354

McMahon, H.T., Y.A. Ushkaryov, L. Edelmann, E. Link, T. Binz, H. Niemann, R. Jahn, and T.C. Südhof. 1993. Cellubrevin is a ubiquitous tetanus-toxin substrate homologous to a putative synaptic vesicle fusion protein. *Nature.* 364:346–349. https://doi.org/10.1038/364346a0

Menon, S., N.P. Boyer, C.C. Winkle, L.M. McClain, C.C. Hanlin, D. Pandey, S. Rothenfußer, A.M. Taylor, and S.L. Gupton. 2015. The E3 Ubiquitin Ligase TRIM9 Is a Filopodia Off Switch Required for Netrin-Dependent Axon Guidance. *Dev. Cell.* 35:698–712. https://doi.org/10.1016/j.devcel.2015.11.022

Miesenböck, G., D.A. De Angelis, and J.E. Rothman. 1998. Visualizing secretion and synaptic transmission with pH-sensitive green fluorescent proteins. *Nature.* 394:192–195. https://doi.org/10.1038/28190

Mostov, K.E., M. Verges, and Y. Altschuler. 2000. Membrane traffic in polarized epithelial cells. *Curr. Opin. Cell Biol.* 12:483–490. https://doi.org/10.1016/S0955-0674(00)00120-4

Oishi, Y., T. Arakawa, A. Tanimura, M. Itakura, M. Takahashi, Y. Tajima, I. Mizoguchi, and T. Takuma. 2006. Role of VAMP-2, VAMP-7, and VAMP-8 in constitutive exocytosis from HSY cells. *Histochem. Cell Biol.* 125:273–281. https://doi.org/10.1007/s00418-005-0068-y

Okabe, A., and I. Yamada. 2001. The K -Function Method on a Network and its computational implementation. *Geogr. Anal.* 33:270–290.

Paul, L.K., W.S. Brown, R. Adolphs, J.M. Tyszka, L.J. Richards, P. Mukherjee, and E.H. Sherr. 2007. Agenesis of the corpus callosum: genetic, developmental and functional aspects of connectivity. *Nat. Rev. Neurosci.* 8:287–299. https://doi.org/10.1038/nrn2107

Pawley, J. 1990. Fundamental limits in confocal microscopy. In Handbook of Biological Confocal Microscopy. Springer Science + Business Media LLC, New York. 15–26.

Pearse, B.M. 1976. Clathrin: a unique protein associated with intracellular transfer of membrane by coated vesicles. *Proc. Natl. Acad. Sci. USA.* 73:1255–1259. https://doi.org/10.1073/pnas.73.4.1255

Petersen, J.D., S. Kaech, and G. Banker. 2014. Selective microtubule-based transport of dendritic membrane proteins arises in concert with axon specification. *J. Neurosci.* 34:4135–4147. https://doi.org/10.1523/JNEUROSCI.3779-13.2014

Pfenninger, K.H. 2009. Plasma membrane expansion: a neuron's Herculean task. *Nat. Rev. Neurosci.* 10:251–261. https://doi.org/10.1038/nrn2593

Pfenninger, K.H., and L.B. Friedman. 1993. Sites of plasmalemmal expansion in growth cones. *Brain Res. Dev. Brain Res.* 71:181–192. https://doi.org/10.1016/0165-3806(93)90170-F

Plooster, M., S. Menon, C.C. Winkle, F.L. Urbina, C. Monkiewicz, K.D. Phend, R.J. Weinberg, and S.L. Gupton. 2017. TRIM9-dependent ubiquitination of DCC constrains kinase signaling, exocytosis, and axon branching. *Mol. Biol. Cell.* 28:2374–2385. https://doi.org/10.1091/mbc.E16-08-0594

Popov, S., A. Brown, and M.M. Poo. 1993. Forward plasma membrane flow in growing nerve processes. *Science.* 259:244–246. https://doi.org/10.1126/science.7678471

Protopopov, V., B. Govindan, P. Novick, and J.E. Gerst. 1993. Homologs of the synaptobrevin/VAMP family of synaptic vesicle proteins function on the late secretory pathway in S. cerevisiae. *Cell.* 74:855–861. https://doi.org/10.1016/0092-8674(93)90465-3

Ripley, B.D. 1976. The Second-Order Analysis of Stationary Point Processes. *J. Appl. Probab.* 13:255–266. https://doi.org/10.1017/S0021900200094328

Ros, O., T. Cotrufo, R. Martínez-Mármol, and E. Soriano. 2015. Regulation of patterned dynamics of local exocytosis in growth cones by netrin-1. *J. Neurosci.* 35:5156–5170. https://doi.org/10.1523/JNEUROSCI.0124-14.2015

Schmoranzer, J., G. Kreitzer, and S.M. Simon. 2003. Migrating fibroblasts perform polarized, microtubule-dependent exocytosis towards the leading edge. *J. Cell Sci.* 116:4513–4519. https://doi.org/10.1242/jcs.00748

Sebastian, R., M.-E. Diaz, G. Ayala, K. Letinic, J. Moncho-Bogani, and D. Toomre. 2006. Spatio-temporal analysis of constitutive exocytosis in epithelial cells. *IEEE/ACM Trans. Comput. Biol. Bioinform.* 3:17–32. https://doi.org/10.1109/TCBB.2006.11

Serafini, T., T.E. Kennedy, M.J. Galko, C. Mirzayan, T.M. Jessell, and M. Tessier-Lavigne. 1994. The netrins define a family of axon outgrowth-promoting proteins homologous to C. elegans UNC-6. *Cell.* 78:409–424. https://doi.org/10.1016/0092-8674(94)90420-0

Shaner, N.C., M.Z. Lin, M.R. McKeown, P.A. Steinbach, K.L. Hazelwood, M.W. Davidson, and R.Y. Tsien. 2008. Improving the photostability of bright monomeric orange and red fluorescent proteins. *Nat. Methods.* 5:545–551. https://doi.org/10.1038/nmeth.1209

Söllner, T., M.K. Bennett, S.W. Whiteheart, R.H. Scheller, and J.E. Rothman. 1993. A protein assembly-disassembly pathway in vitro that may correspond to sequential steps of synaptic vesicle docking, activation, and fusion. *Cell.* 75:409–418. https://doi.org/10.1016/0092-8674(93)90376-2

Stefan, C.J., A.G. Manford, and S.D. Emr. 2013. ER-PM connections: sites of information transfer and inter-organelle communication. *Curr. Opin. Cell Biol.* 25:434–442. https://doi.org/10.1016/j.ceb.2013.02.020

Taylor, A.M., S. Menon, and S.L. Gupton. 2015. Passive microfluidic chamber for long-term imaging of axon guidance in response to soluble gradients. *Lab Chip.* 15:2781–2789. https://doi.org/10.1039/C5LC00503E

Tojima, T., H. Akiyama, R. Itofusa, Y. Li, H. Katayama, A. Miyawaki, and H. Kamiguchi. 2007. Attractive axon guidance involves asymmetric membrane transport and exocytosis in the growth cone. *Nat. Neurosci.* 10:58–66. https://doi.org/10.1038/nn1814

Tojima, T., R. Itofusa, and H. Kamiguchi. 2014. Steering neuronal growth cones by shifting the imbalance between exocytosis and endocytosis. *J. Neurosci.* 34:7165–7178. https://doi.org/10.1523/JNEUROSCI.5261-13.2014

Viesselmann, C., J. Ballweg, D. Lumbard, and E.W. Dent. 2011. Nucleofection and primary culture of embryonic mouse hippocampal and cortical neurons. *J. Vis. Exp.* 47:2373.

Vincent, L. 1993. Morphological grayscale reconstruction in image analysis: applications and efficient algorithms. *IEEE Trans. Image Process.* 2:176–201. https://doi.org/10.1109/83.217222

Watanabe, S., B.R. Rost, M. Camacho-Pérez, M.W. Davis, B. Söhl-Kielczynski, C. Rosenmund, and E.M. Jorgensen. 2013. Ultrafast endocytosis at mouse hippocampal synapses. *Nature.* 504:242–247. https://doi.org/10.1038/nature12809

Waters, J.C. 2009. Accuracy and precision in quantitative fluorescence microscopy. *J. Cell Biol.* 185:1135–1148. https://doi.org/10.1083/jcb.200903097

Wen, P.J., S. Grenklo, G. Arpino, X. Tan, H.-S. Liao, J. Heureaux, S.-Y. Peng, H.-C. Chiang, E. Hamid, W.-D. Zhao, et al. 2016. Actin dynamics provides membrane tension to merge fusing vesicles into the plasma membrane. *Nat. Commun.* 7:12604. https://doi.org/10.1038/ncomms12604

Winckler, B., P. Forscher, and I. Mellman. 1999. A diffusion barrier maintains distribution of membrane proteins in polarized neurons. *Nature.* 397:698–701. https://doi.org/10.1038/17806

Winkle, C.C., L.M. McClain, J.G. Valtschanoff, C.S. Park, C. Maglione, and S.L. Gupton. 2014. A novel Netrin-1–sensitive mechanism promotes local SNARE-mediated exocytosis during axon branching. *J. Cell Biol.* 205:217–232. https://doi.org/10.1083/jcb.201311003

Winkle, C.C., R.H.J. Olsen, H. Kim, S.S. Moy, J. Song, and S.L. Gupton. 2016. Trim9 Deletion Alters the Morphogenesis of Developing and Adult-Born Hippocampal Neurons and Impairs Spatial Learning and Memory. *J. Neurosci.* 36:4940–4958. https://doi.org/10.1523/JNEUROSCI.3876-15.2016

Yuan, T., J. Lu, J. Zhang, Y. Zhang, and L. Chen. 2015. Spatiotemporal detection and analysis of exocytosis reveal fusion "hotspots" organized by the cytoskeleton in endocrine cells. *Biophys. J.* 108:251–260. https://doi.org/10.1016/j.bpj.2014.11.3462